https://doi.org/10.15407/ufm.26.03.529

B.M. MORDYUK^{1,*}, M.O. VASYLYEV^{1,**}, S.M. VOLOSHKO^{2,***}, and O.A. VYSLYI²

- ¹G.V. Kurdyumov Institute for Metal Physics of the N.A.S. of Ukraine,
- 36 Academician Vernadsky Blvd., UA-03142 Kyiv, Ukraine
- ² National Technical University of Ukraine
- 'Igor Sikorsky Kyiv Polytechnic Institute',
- 37 Beresteiskyi Ave., UA-03056 Kyiv, Ukraine

INCREASING RESISTANCE TO ULTRASONIC CAVITATION EROSION OF METALLIC PARTS BY MEANS OF SURFACE MODIFICATION

The current development of surface treatments, which are aimed at improving the cavitation erosion (CE) resistance of the metal parts working under vibration conditions in liquid environments, is reviewed. The ultrasonic-cavitation test, which is a convenient and express method for evaluating the cavitation resistance of materials, is also considered. The CE resistance of the metal samples is mainly tested using the typical ultrasonic-vibration apparatus according to the ASTM G32-10 test standard. The physical mechanism of the surface cavitation destruction based on the vaporousbubbles' formation is described and analysed. This analysis allows for a better understanding of the role of the surface-treatment methods and their parameters on the structure and mechanical properties of the near-surface region, helping to enhance the protection against the destructive cavitation effects. Examples are given regarding the effective methods for improving the surface-properties' finish of various metal materials, viz., coatings methods including microarc oxidation, arc spraying, high-velocity oxygen-fuel deposition, cold spraying, cathode arc plasma deposition, laser surface alloying, and nitriding. Additionally, the methods of surface modification, such as laser surface treatment, friction stir processing, and tungsten inert-gas welding/dressing, are also concluded to be efficient CE inhibitors.

Keywords: cavitation, surface treatments, coating, erosion resistance, ultrasonic vibration, cavitation tests.

Citation: B.M. Mordyuk, M.O. Vasylyev, S.M. Voloshko, and O.A. Vyslyi, Increasing Resistance to Ultrasonic Cavitation Erosion of Metallic Parts by Means of the Surface Modification, *Progress in Physics of Metals*, **26**, No. 3: 529–566 (2025)

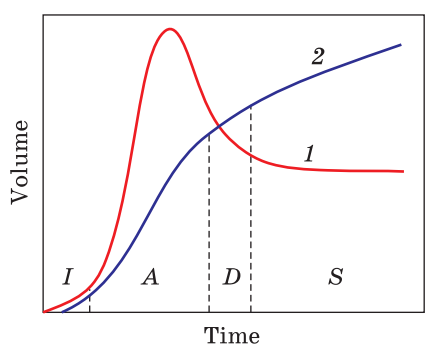
 \odot Publisher PH "Akademperiodyka" of the NAS of Ukraine, 2025. This is an open access article under the CC BY-ND license (https://creativecommons.org/licenses/by-nd/4.0)

^{*}mordyuk@imp.kiev.ua, ** vasil1934@ukr.net, *** voloshkosvetlana13@gmail.com

1. Introduction

1.1. The Cavitation Phenomena

The cavitation and consequent erosion of the solid surface are the physical-chemical phenomena initiated by local pressure fluctuations in the liquid as a local static pressure decreases below some threshold value [1-4]. It was discovered over one hundred years ago. As established in the 1950s, cavitation erosion is the kind of material damage that occurs due to the violent collapses of cavitation bubbles [5-7]. The cyclic impact of the cavitation pulses onto the material surface causes its gradual degradation, which is usually called 'cavitation erosion' (CE). Such a degradation process consists of three main stages (Fig. 1): incubation (I), acceleration (A), deceleration (D) and steady state (S). During the first stage, the material accumulates the impact energy accompanied by the elastic and plastic deformation of the near-surface region. As a result of this process, the properties of the surface layer changed significantly. The next acceleration period contributes to the intensive material loss. At the end of this stage, the erosion rate achieves its maximum degree. The surface erosion extends over the entire area subjected to the cavitation. Gradual changes in the surface geometry led to the beginning of the next period, which is characterized by a progressive decrease in the erosion rate. The last period of the surface degradation is a steady-state one, during which the erosion rate is almost constant due to slight changes in the surface geometry and structure. In the incubation period, the slip bands and plastic deformation-induced pits at the material surface are observed and the deformation level increases with the cavitation time. The repeated impacts of the cavitation pulses also lead to the surface hardening and initiation of several microcracks, which over time turn into macrocracks and consequently to the material mass loss. As a result, the geometry of the material surface changes and decelerates the degradation process leading to a steady-state cavitation period. Note that the processes surrounding the cavitation erosion of material surface are highly complex, and they are associated with the microplastic deformation and the stress fields generated as a result of the cavitation-bubbles' collapse close to the surface.



CE depends on the physical and chemical properties of the liquid and affected material, as well as on the cavitation development called 'cavitation intensity', which can be expressed by the equation [9]

Fig. 1. Curves of the material surface degradation during cavitation: 1 denotes a volume (mass) loss; 2 is a volume (mass) loss rate [8]

$$I = \frac{K}{T} \frac{1}{2pc} \sum_{k=1}^{M} n_k p_k^2$$
,

where $K=10^{-5}$ is a proportionality coefficient, T is a total measurement time, r is a liquid density, c is sound velocity, M is a number of the pressure intervals, k is the consecutive number of the interval, n_k is a number of pulses in the interval, p_k is a value of the pressure amplitudes in the k-th interval.

1.2. Cavitation Erosion Mechanism

In the 1950s, it was established that cavitation erosion was the kind of damage that was caused by the violent collapses of the cavitation bubbles. The mechanism of the cavitation erosion can be described as follows [1-4]. As usual, the liquid will contain either gaseous or vaporous bubbles, which can serve as the cavitation nuclei. The bubbles become the storage of the vapour or dissolved gases, when the pressure is reduced to a certain level. As a result, the bubbles increase rapidly in size. Subsequently, when the bubbles enter the reduced pressure zone, they are reduced in size due to vapour condensation. Such condensation process takes place fairly quickly and is accompanied by local hydraulic shocks, the emission of sound, the destruction of the surface material bonds and other undesirable phenomena. It was established that the volumetric stability reduction in most liquids is associated with the contents of the various admixtures, such as the solid nonwettable particles and gas-vapour bubbles. It is particularly on the submicron level, which serves as the cavitation nuclei. A critical aspect of the CE process is the destruction of material surface and material displacement, which is caused by high relative motions between the surface and the exposed fluid. During such motions, the fluid local pressure is reduced. As a result, the temperature of the liquid reaches the boiling point, and small vapour cavities are formed.

The two main CE mechanisms were suggested: 1) the formation of the shock waves emitted into the fluid (I and II) and 2) if the bubble collapses close enough to the solid surface, the microjet phenomenon occurs (III and

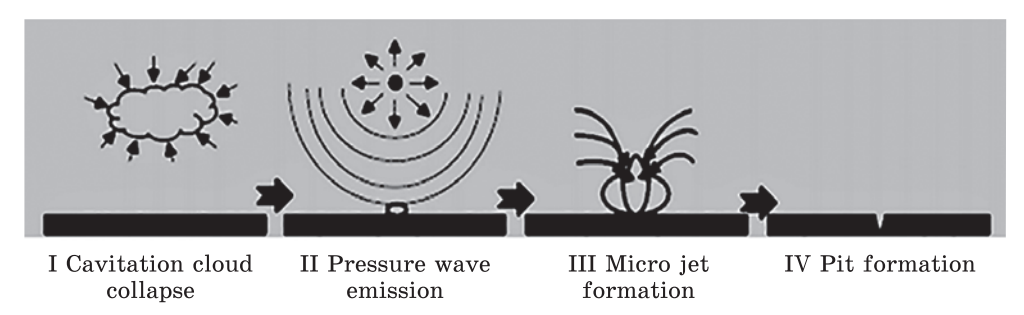


Fig. 2. Schematic view of micro-jet and shock wave formations and their effects [8]

IV), as shown in Fig. 2. The outcome of the microjet impacts by the solid surface is the formation of the single pits [8, 11]. Thus, the CE is a complex phenomenon, involving the complicated flow phenomena combined with the reaction of the particular material of which the solid surface is composed.

1.3. Cavitation and Technique

The main result of the cavitation is the mass loss of the material, known as CE. This phenomenon can be both harmful and useful in practical terms. The mass loss due to cavities' formations reduces the lifetime of the machine parts and/or equipment, which can cause catastrophic collapse [11–13]. The damage caused by the CE gradually extravagates in many industry fields, such as overflow components of the metallurgical, petrochemical, mineral mining and separation, water conservancy, transportation and deep-sea mining vehicles [14, 15]. In addition, it was demonstrated that the CE is a general phenomenon in such fields as aviation, navigation, the hydraulic turbine of the hydropower station, the rudder blade or arm of a high-speed vessel, and the afterburner fuel pump of the aeroengine [16–19]. Therefore, the phenomenon of CE constantly attracts extensive attention both in academic research and in industrial applications. This includes numerous studies on using this phenomenon to modify metal surfaces to increase their hardness and wear resistance [20–26].

The CE resistance of bulk metallic materials is enhanced by increasing their mechanical properties, *i.e.*, hardness, tensile strength, yield strength, strain energy, fracture toughness, and fatigue strength. Additionally, the highest CE and corrosion resistance were reported for materials with homogeneous and fine-grained structures [4, 27–29]. Therefore, to predict the erosion rate, it is important to determine the relationship between the material properties and their cavitation dwell with resistance.

1.4. Ultrasonic Cavitation

The special type of cavitation is ultrasonic cavitation. The peculiarity of this phenomenon is the emergence of nonlinear time-varying acoustic waves, which are induced by vibrations propagated into the liquid medium. Ultrasonic cavitation is sometimes called acoustic cavitation. Ultrasonic cavitation, as a nonlinear acoustic phenomenon, involves the dynamic processes of expansion, oscillation, compression, and collapse in the liquid medium [30–34]. High-power ultrasound enhances the rate of the various physical and chemical processes in such a liquid medium through the generation and subsequent collapse of the cavitation bubbles. The CE induced by ultrasonic waves involves the transmission of the sound waves within the ultrasonic frequency spectrum, which equals or exceeds 20 kHz, through the liquid medium. The cavities in the liquid or bubbles form and

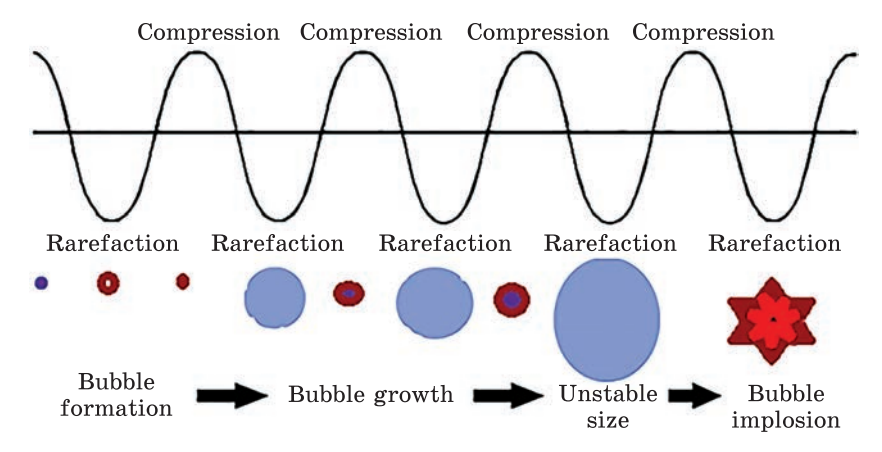


Fig. 3. Schematic view of the ultrasonic cavitation [35]

grow when negative-pressure amplitude drops to or below the vapour pressure of the liquid. Subsequently, these bubbles' collapses during the cycle of positive pressure generate the high-pressure shockwaves and microjets. More precisely, the bubbles formed in the low-pressure regions are filled with vapour or dissolved gases that implode after their formation, which can be very violent in the higher-pressure areas. During the implosion of the bubbles, the microjets and shock waves are generated. In summary, the cavitation phenomenon consists of three distinct steps of the bubble nucleation (formation),

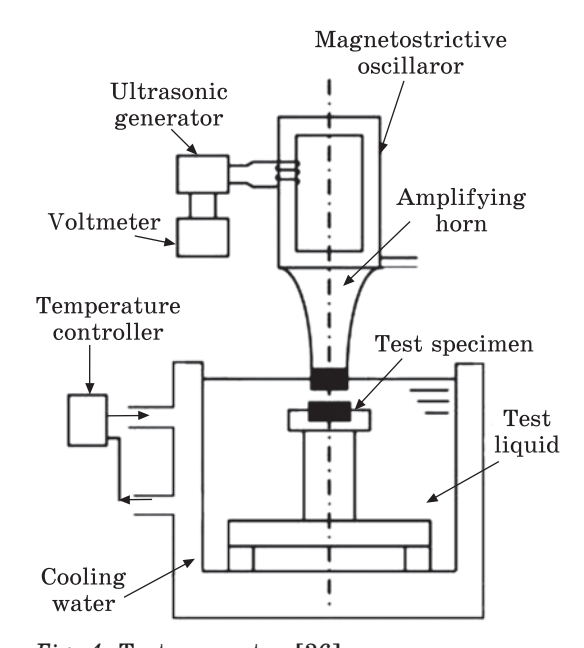


Fig. 4. Test apparatus [36]

rapid growth and expansion to the critical size during alternating cycles of compression—rarefaction, and implosion and violent collapse of the bubble in the liquid (Fig. 3).

The Cavitation Test Method. The CE resistance of the metal samples is tested using the typical ultrasonic vibration apparatus, as shown in Fig. 4 (according to the ASTM G32-10 test method). The cavitation process in the liquid medium can be generated by an ultrasonic horn supplied either by magnetostrictive or piezoelectric transducers. When ultrasonic

vibrations are switched on, the cylindrical cavitation cloud (bubbles) occurs between the sample and the horn tip. The amplifying horn, which is usually titanium-made, is the oscillator. The most commonly used liquid medium is the tap water, the distilled water or the NaCl solution, which are kept at 18–25 °C. The vibration frequency of the horn is in the range of 20–40 kHz.

1.5. Ultrasonic Cavitation and Surface Modification

With the progress of modern science and technology, ultrasonic cavitation technology has been applied in many fields, such as mechanical processing, biomedicine, modification of the solid surface, chemical engineering, dispersion and mechanical alloying of metallic powders, and so on [37-43]. The cavitation pitting of solid surfaces is also applied in many industrial fields, i.e., ultrasonic cleaning and metal surface hardening. The impact force affecting the material surface is formed due to the collapse of the cavitation bubble, which leads to the phase transition and plastic deformation in the near-surface layers of the material. CE has a detrimental effect on the material performance while having a positive influence on the surface hardness [44-47]. One of the most popular applications of ultrasonic cavitation is the execution of the cavitation tests of the materials to the quantitative description of the relationship between the CE characteristics in the controlled environment and the material properties. As a rule, the material resistance to the CE is graphically presented by the mass/volume loss vs. time dependence, or erosion rate during the exposure period in the controlled liquid medium. Such an erosion test is significantly more accelerated than the actual cavitation that the studied material will be subjected to (so far, using either a much higher repetition rate of the cavitation events, more energetic events, more developed cavitation, or a combination of these). The laboratory techniques include using ultrasonic vibrations to generate cavitation and related phenomena, i.e., the cavitation flow loops with strong separating flows, rotating disks, venture cavitation flows, vortex generators, and submerged cavitating jets [1-4]. The most commonly used standard procedure for determining material resistance to CE is the ASTM G32-16 test method [8, 48].

The erosion loss of the materials was expressed in terms of the mean depth of erosion (MDE) and the mean cavitation erosion rate (MCER), as calculated according to the following equations:

$$\text{MDE} = \frac{\Delta W}{10\rho A}, \text{ MCER} = \frac{\Delta W}{10\rho A \Delta t};$$

here, ΔW is the weight loss in mg, Δt is the time interval in h, A is the eroded area in cm², and r is the density of the modified layer in g/cm³. In

addition, CE resistance $R_{\rm e}$ is defined as the reciprocal of the MCER [8]:

$$R_{\circ} = (\text{MCER})^{-1}$$
.

Among the many studies concerned with the problem of cavitation, a special place belongs to works devoted to methods for protection against this phenomenon that is harmful to technology. Below, there are examples of the methods for improving the cavitation resistance of the metal surface.

2. Anticavitation Protective Coatings

Over the past few years, metal alloys have been frequently protected from CE-caused damage using hard material coatings that modify the surface properties of the metal. Examples of the most effective methods of applying coatings that significantly improve the CE resistance of the metal surfaces are considered below.

One of the most promising methods for producing protective coatings is microarc oxidation (MAO) [49, 50]. MAO, also known as 'plasma electrolytic oxidation' (PEO) [51], is the electrochemical and electrothermal oxidation in the alkaline electrolyte, where the oxidation of a material surface is driven by the supply of high voltage (up to 600 V) pulsed AC power. MAO has attracted substantial attention, as the method is effective for the surface coating methodology. The MAO coatings exhibited high hardness, good adhesion, excellent corrosion and wear resistance. For example, the formation of such coatings with excellent properties is the modern way to address poor wear and CE resistance of aluminium alloys [52]. That work contributed to understanding the reasons for the high CE resistance of the MAO coatings. It also provides essential results on the overall potential of MAO ceramic coatings as the future solution for elements of machines and devices exposed to cavitation loads produced from the aluminium alloy 5056 (in wt. %: Cu 0.10, Mg 5.35, Fe 0.4, Si 0.32, Zn 0.1, Ti 0.15, Cr 0.18, Al rest). To produce the MAO coatings, an aqueous solution of 2 g/L KOH and 5 g/L Na,SiO, was applied as the electrolyte. The electrolyte temperature was controlled at 25-30 °C throughout the

process. The MAO treatment was carried out using the pulsed AC power source using the following parameters: the current density, voltage, frequency, duty cycle, and duration time were 25 A/dm², 280 V, 50 Hz, 50% and 60 min, respectively. The cavitation tests were made by a vibratory cavita-

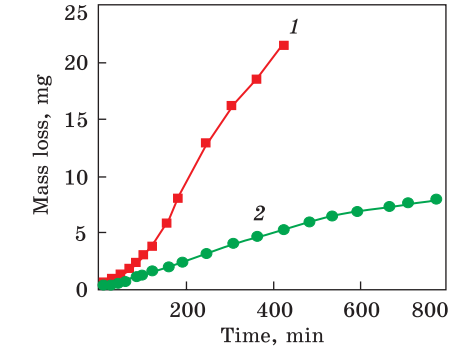


Fig. 5. Cumulative mass loss for Al alloy 5056 (1), and MAO coating (2) [52]

Coatings	$t_{ m ine}$, min	MCER, mg/min	$t_{\rm \tiny MCER}$	$\Delta_{ m m}$	(MCER) ⁻¹	R
MAO	80	0.031	120	5.5	32.25	3.95 1
Al alloy	0	0.087	240	21	11.49	

Table 1. Characteristic values of the cavitation tests [52]

tion apparatus Hielscher UP400s (400 W, 24 kHz, 110 μ m peak to peak amplitude in the distilled water at 22 °C) according to the ASTM G32-10 tests method recommendations.

As a result of the MAO process, Al_2O_3 (g- Al_2O_3 phase) coatings with different structures were obtained depending on the material covering the 5056 aluminium alloy substrates. Figure 5 shows the course of CE curves. Several characteristics of the material destruction stages can be distinguished, namely, the incubation period ($\tau_{\rm inc}$), for which there is no mass loss; the period of the increasing cavitation erosion rate; and the maximum stage. The main results are listed in Table 1.

2.1. Arc-Sprayed Coatings

In recent years, considerable efforts have been devoted to investigating the CE behaviour of Fe-based amorphous/nanocrystalline coatings. Such coatings prepared by thermal spraying have been widely adopted by hydraulic machinery, power plants and coastal installations because of their desirable combination of relatively low material cost, high hardness and toughness, and outstanding corrosion and wear resistance [53, 54]. As shown, the material surface roughness plays an important role in the CE process. In the study [55], this factor was quantified using the example of the CE behaviour of the FeCr19C0.1B1.6 (at.%) amorphous/nanocrystalline coating prepared by arc spraying process on the stainless steel 1Cr18Ni9Ti selected as the substrate. The following arc spraying parameters were used: the spraying voltage of 36 V; the wire feed rate of 2.7 m/ min; the compressed air pressure of 700 kPa; and a gun traverse speed of 100 mm/s. The thickness of the obtained coating was of about 230 μ m. The operating parameters of the cavitation test according to the ASTM G32-10 standard were as follows: the vibration frequency was of 19 kHz; peakto-peak amplitude was of 60 µm; the power of the ultrasonic generator was of 250 W.

The cross-sectional microstructure of the FeNiCrBSiNbW amorphous/nanocrystalline coating is shown in Fig. 6. It can be seen from the overall view in Fig. 6, a, the coating is dense and has the typical lamellar structure with an average thickness of 230 μ m. There is a good adherence to the substrate owing to the uniform and compact interface between the substrate and the coating layer. At high magnification (Fig. 6, b), one can see some pores (less than 2%), the unmelted particles and the microcracks.

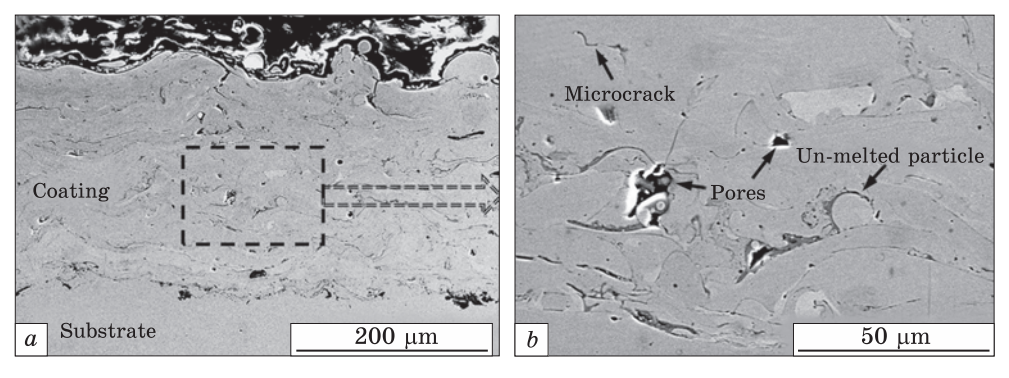
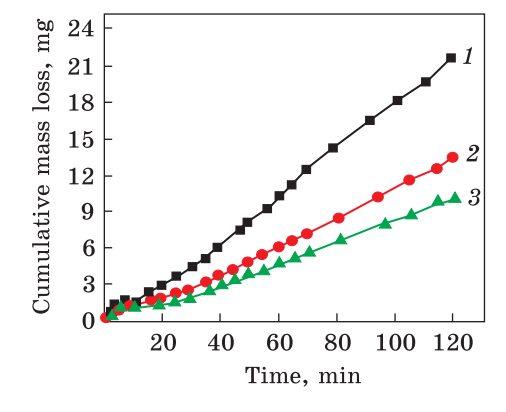


Fig. 6. Scanning electron microscopy images of the cross-section of the as-sprayed FeNiCrBSiNbW coating: a — the overall view morphology, and b — the magnification of the rectangular frame in a [55]

Fig. 7. The relationship between cumulative mass loss and CE time for the assprayed FeNiCrBSiNbW coatings with three surface roughness levels: 80 (1), 600 (2), and 1000 (3) grit grinding [55]

Besides the pores, appearing as black regions, the coating consists of bright white region, grey region, and dark grey region. The grey region is primarily a coating alloy with the chemical composition of Fe71Ni5Cr15B3 Si3Nb2W1 (at.%). The bright white



region and the dark grey region are the W-rich phase and the iron oxide phase, respectively. TEM shows the nanocrystalline grains with dimensions ranging from 70 nm to 130 nm are uniformly distributed in the amorphous matrix.

Figure 7 shows the relationship between cumulative mass loss and CE time for the FeNiCrBSiNbW amorphous/nanocrystalline coatings with three surface roughness levels. The results show a considerable difference in the mass loss rate of the as-sprayed coatings under three different surface conditions (*i.e.*, 80, 600, and 1000 grit grinding). At the same time, the mass losses of all three coating specimens increase with the test time. The incubation period is not observed for all three coating specimens, which reflects that the surface conditions in this study put the coatings one-step ahead of the CE damage process. The coating after 80 grit grinding exhibits the greater mass loss (21.8 mg), while the coating after 1000 grit grinding has the lower mass loss (10.3 mg) after 120-min test. Furthermore, the mass loss data of the coating after 600 grit grinding are very close to that of the coating after 1000 grit grinding during the first

30 min, but gradually higher than data are after 1000 grit grinding, when the test time exceeds 30 min. This is because the higher the surface roughness, the higher the density of the bubbles nucleated near the surface of the coated specimen. Thus, the collapsing bubbles exert more impact on the surface, and much more mass loss is observed.

2.2. High Velocity Oxy-Fuel Spraying

High velocity oxy-fuel (HVOF) is a thermal spray coatings process that uses a mixture of fuel gas and oxygen to produce a high-velocity flame. This flame is then used to heat and accelerate the stream of powdered material onto the surface of the substrate, where it melts and forms the coating. This method produces a coating that is extremely dense and well bonded to the substrate. This makes it ideal for applications that require superior protection against abrasion and corrosion, as well as high-temperature environments, including aerospace, automotive, oil and gas, and many others. Usually, the HVOF coatings are less porous, show a low degree of oxidation and hardness, and have higher bond strength than other thermal spraying methods [56–59]. In particular, the next works have demonstrated that HVOF is an effective technique to reduce the CE of the metal parts.

The aim of the work [60] was to study the effects of the mechanical properties and the microstructure on tribological behaviour and CE resistance of the different cermet coatings deposited onto AZ31 magnesium alloy by HVOF spraying. Three commercial tungsten carbide-based powders were employed: WC–Co–Cr, WC–Co, and WC–Cr $_3$ C $_2$ –Ni. The following spray parameters were used for deposition of the coatings: oxygen flow rate of 900 slpm, kerosene flow rate of 26 l/h, nitrogen flow rate of 12 slpm, powder feed rate of 70 g/min, water flow rate of 23 slpm, and spray distance of 360 mm. The average thickness of the as-sprayed coatings was in the range from about 184 up to 258 µm. The CE was generated by the magnetostriction-driven apparatus (20 kHz) with peak-to-peak amplitude of 50 µm. The MDE and the MER values are listed in Table 2.

As seen, the WC-Co-Cr coatings gave superior CE resistance and had the lowest volume loss, which successfully mitigated erosion wear. The

CE results	WC-Co-Cr	WC-Co	$ \overline{ \text{WC-Cr}_3 \text{C}_2 \text{-Ni} } $	AZ31
Cumulative mass loss, mg	52.18	145.62	89.21	192.74
MDE, µm	19.50	53.64	36.44	567.15
MER, µm/h	3.76	12.76	8.61	144.48
Volume loss, mm³	3.74	10.30	6.99	108.82

Table 2. The MDE and the MER values as the cavitation test results [60]

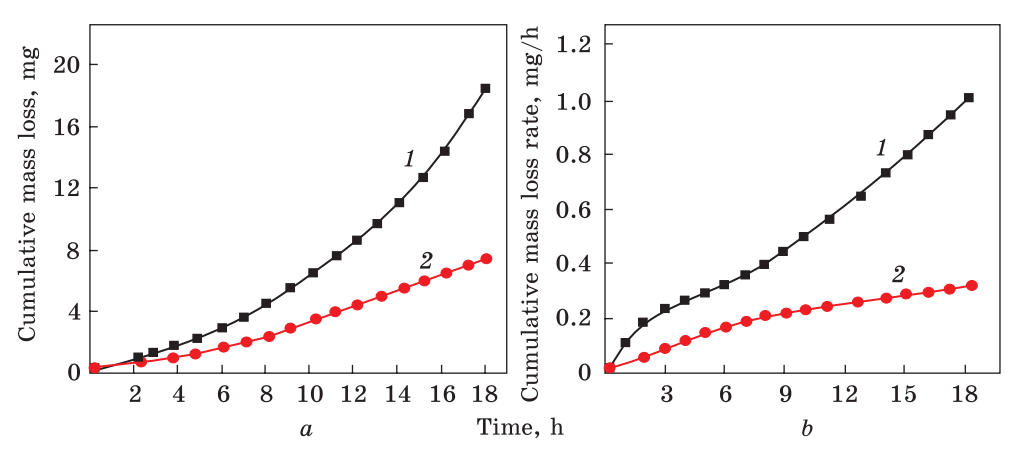


Fig. 8. Cumulative ML (a) and MLR (b) vs. CE time of the coating and NAB in the distilled water [60]

WC-Co-Cr coating had 1.8 times lower MDE than that of WC-Cr $_3$ C $_2$ -Ni coating and 2.8 times higher CE resistance than that of WC-Co one. All the tested cermets gave at least 10 times lower MDE than that of the reference AZ31 sample. The WC-12Co coatings sprayed by HVOF with different WC sizes were studied in [61].

Ship propellers suffered from serious coupling damage by CE when operated at high speed in the marine environment. To improve the CE resistance of the Ni–Al bronze (NAB) propeller alloy, the novel Cu-based medium-entropy alloy (MEA) (Cu55Al20Ni12Ti8Si5, at.%) coating was prepared by HVOF spraying technology in the study [62]. The optimized coatings parameters are identified as 802.3 L/min of oxygen flow, 0.38 L/min of kerosene flow, 320 mm of spray distance, 280 mm/s of spray gun speed, 10.86 L/min of argon carrier gas flow rate and 5.5 rpm of the Cu-based MEA powder feed rate. Cavitation was generated by the ultrasonic generator with resonance frequency of 20 kHz and vibration amplitude of 60 µm. The distilled water was selected as the experiment environment.

XRD patterns for the as-sprayed coating and the NAB show that the coating contains only the b.c.c. solid solution phase. The coating was about 367 µm thick. The coating exhibits much higher hardness (HV = 6.73 GPa), and lower elastic modulus (E = 136.1 GPa) than those of the NAB. Figure 8 demonstrates the cumulative mass loss (ML) and the mass loss rate (MLR) vs. CE time for the coating and NAB. As seen, both coating and NAB exhibit no significant ML in the distilled water even when CE time achieves up to 4 h (this time can be regarded as the CE incubation period). However, when the cavitation time increases up to 10 h, the ML of the NAB increases quickly and becomes significantly higher than that of the coating. The cumulative ML and MLR of the NAB (19.1 mg and 1.06 mg/h) are 2.6 times regarding that of the coating (7.3 mg and 0.41 mg/h) after CE for 18 h, which

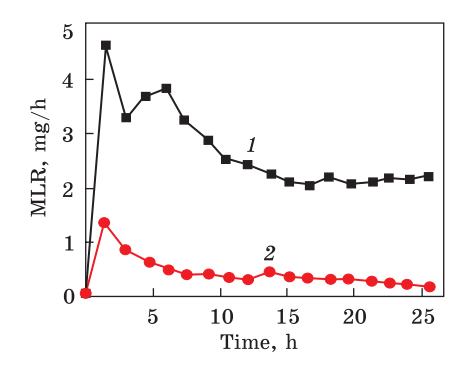


Fig. 9. Curves of the mass loss rates versus time for the AISI 321 steel (1) and Fe-based coating (2) [65]

illustrates much better CE resistance of the coating in distilled water. Thus, the coating is expected to have better CE resistance than the NAB.

It is well known that amorphous metal alloys have several unique prop-

erties due to their disordered structure. However, the application of these amorphous solids in the technology has been restricted due to their inherent drawbacks, such as high fabrication cost, small-sized parts due to technical difficulties and apparent room temperature brittleness [63]. In this regard, it is proposed to use coating materials such as iron-based alloys, which have a good combination of strength and toughness, as well as wear and corrosion resistance [64]. Due to their unique structure and properties, Fe-based amorphous/nanocrystal coatings may have great potential for CE resistance applications. Among various thermal spray processes, HVOF spraying is reported to be a flexible and versatile technology to prepare high-quality amorphous and/or nanocrystalline coatings [65]. In that work, the ultrasonic CE behaviour of the coating deposited under the optimal HVOF spray parameters was studied. The Fe-based alloy powder used in that study was the commercially available powder with the chemical composition of (43.0-46.0 wt.% Cr, 5.6-6.2 wt.% B, 1.75-2.25wt.% Si, 0.17 max wt.% C, 0.02 max wt.% S, and the balance Fe), and the size distribution of 15-45 µm. The feedstock powder was coated on the substrate of AISI 321 steel by the commercial HVOF thermal spraying system. The spray parameters were maintained at the powder feed rate of 8 g/min, the spray gun speed of 500 mm/s, and the argon carrier gas flow rate of 10.5 L/min during the experiment. The CE tests were carried out using the vibratory ultrasonic cavitation equipment according to ASTM Standard G32-10 with a frequency of 19 kHz and double (peak-topeak) amplitude of 60 µm [33].

Figure 9 shows the mass loss rates vs. CE time for the HVOF sprayed Fe-based coating deposited on the AISI 321 steel at room temperature. It is also clear that the AISI 321 steel exhibited a higher mass loss rate at each time interval than the Fe-based coating. The mass losses after the cavitation for 27 h of the Fe-based coating and the AISI 321 steel were 10 mg and 60 mg, respectively. That is, the Fe-based amorphous/nanocrystalline coating prepared by HVOF exhibited better CE resistance than the AISI 321 steel. This is mainly explained by the fact that the hardness of the Fe-based coating $(HV_{0.2}=1121)$ is nearly 5 times that of the AISI 321 steel $(HV_{0.2}=260)$.

2.3. Cold Spray Coatings

The cold spray technique has been extensively used for the fabrication of coatings to enhance the surface properties of metallic materials [66-68]. In the work [67], In718 nickel superalloy was used as the reinforcement material within the ductile pure Ni matrix for cold spray. The authors aimed to use the cold spray technique with high pressure for the manufacturing of the composite coating to achieve the enhancement of Ni coating erosion properties and the avoidance of helium used for the deposition of In 718. The produced cold-sprayed coatings were studied in terms of the microstructure and CE to investigate their potential use in the relevant applications. The spherical Ni (16 µm) and In718 (15 µm, LPW) were used as the powder feedstock in this study. Stainless steel 2205 specimens were used as the substrate material. The two powders were mechanically blended at equivalent volume ratios before spraying. Nitrogen was used as the propellant gas at a pressure of 3.0 MPa and a preheating temperature of 900 °C. The powders were fed into the system from the powder hopper (PF100WL, Uniquecoat Technologies LLC, USA) with a feed rate of 210 and 234 g/min for the Ni and the Ni-In718, respectively. The CE tests were implemented using the vibratory apparatus according to the ASTM G32. The frequency of the vibrations was set at 20 kHz, and their amplitude at the top of the ultrasonic transformer at 50 µm. The mass loss and the degradation level were measured during the testing at preselected time intervals, i.e., 30, 60, 90, 120, 150, 180, and 240 minutes.

The basic variables used for the evaluation of the CE resistance of both the Ni and the Ni-In718 coatings were the mass loss (Fig. 10). It is evident that the superiority of the cold sprayed composite deposit becomes more intense especially between 90-180 min of exposure when its mass loss tends to stabilize while the pure Ni mass loss increases exponentially.

The CE demonstrated different features. The mass removal in the case of the Ni coating mainly resulted from the formation of the craters with irregular contours (Fig. 11, a). However, on the composite coating surface, the aforementioned feature was accompanied by the coexistence of intense interparticle microcracks with the particle boundaries (Fig. 11, b).

Probably, these particles are mainly In718, which protrude intact from the Ni matrix. Repeated bubble collapse may cause damage accumulation at two regions, within the particles and at the interparticle boundaries leading to partial

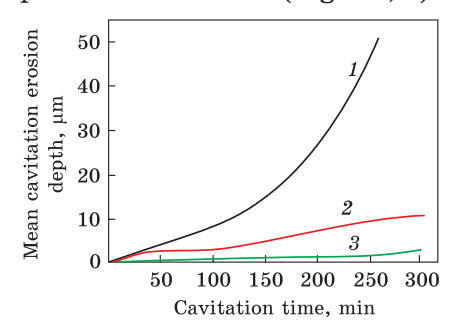


Fig. 10. Comparative CE results for Ni (1) and Ni-In718 coatings (2) [67]

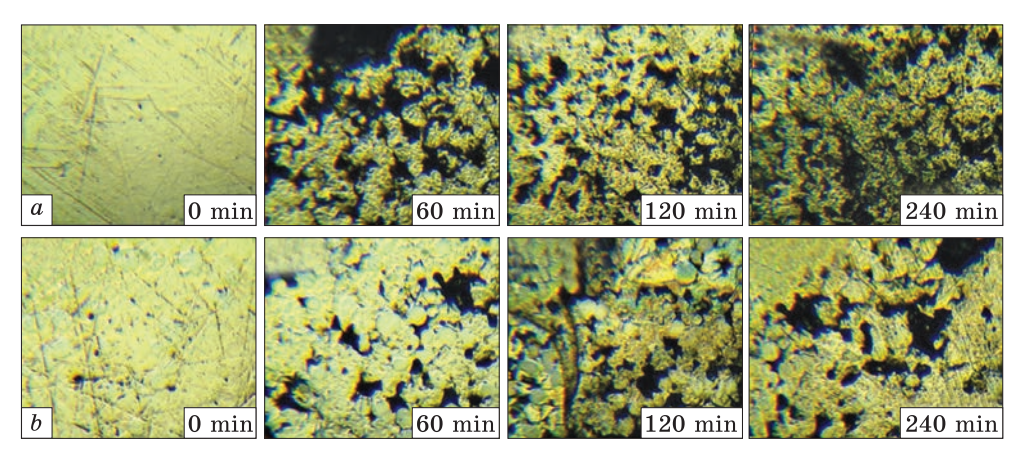


Fig. 11. Macrographs of the eroded surfaces of the pure Ni (a) and Ni-In718 (b) coatings [67]

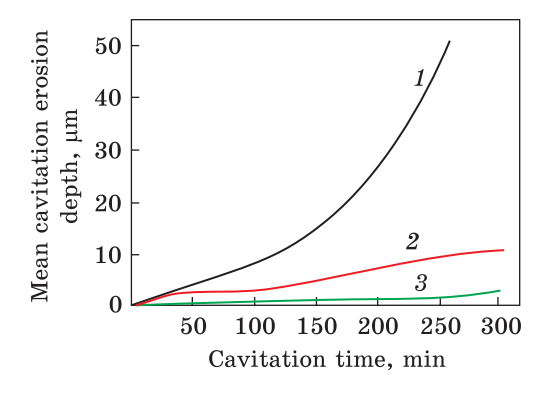


Fig. 12. CE depth for differently processed coatings and the bulk reference material over the exposure time: 1—steel GL-a; 2— $T_{\rm sub}$ = 300 °C; 3—cast CuAl10Fe5Ni alloy [69]

and complete particle removal, respectively. It should be noted that the existence of In718 in the composite coating appears to impede the second mechanism of the mass

loss behaviour, reducing the sites prone to detachment due to its enhanced CE resistance.

The study [69] demonstrates that cold-sprayed bronze coatings have a high potential for ensuring good performance in the rudder protection of the classified shipbuilding steel GL-A with the composition (wt.%): Si 0.186, C 0.056, Cr 0.03, Cu 0.013, Ni 0.013, P 0.011; S 0.006, N 0.0041, Mo 0.002, Fe balance. The present study investigates the coating formation by cold spraying gas-atomized CuAl10Fe5Ni5 bronze powders. The cavitation tests were performed according to ASTM G32-10 with a frequency of 20 kHz and amplitude of 25 µm. The temperature of the distilled water was kept at 22 °C.

Figure 12 displays the developments of the mean cavitation-erosion depths for the cold-sprayed bronze coatings for the bulk references steel GL-A and the cast CuAl10Fe5Ni5. There are typical trends for materials with a long incubation time of about 100 min for the steel and about 250 min for the cavitation-resistant cast nickel—aluminium-bronze, followed by a steady cavitation rate. In contrast, the cold-sprayed bronze coatings from the early beginning show high cavitation rates. That differ-

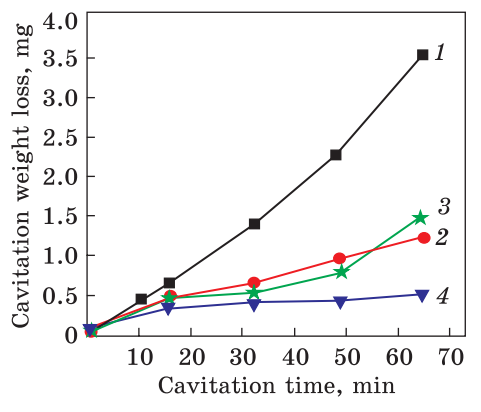
ence can be attributed to the fact that cracks in the bulk material have to be nucleated and spread by repeated deformation of the surface, whereas the cold-sprayed coating already contains crack nuclei. In this comparison, the cast bronze shows the lowest cavitation rates. The differences in the steady state cavitation can be attributed to the material strength and probably toughness to avoid crack growth. As compared to the cast bronze, the higher cavitation rates of the coatings can be attributed to the porosity and the non-bonded internal interfaces, limiting the coating strength and acting as the crack nuclei. The substrate temperature of 300 °C appears as optimum for minimum coating cavitation.

As single impact morphologies show, cold spraying of CuAl10Fe5Ni onto the hard-steel substrates is challenging due to the martensite content in the powder that hinders uniform particle deformation. Cavitation resistance is governed by the coating hardness and quantity of the non-bonded areas that act as the nuclei for material losses. Thus, to achieve the best coating performance, the spray parameters and powder feedstock should be well tuned. In addition, spraying onto heated substrates results in increased substrate deformability, higher bond strength and thermal softening of already adhering layers. Thus, it improves the coating cohesion and, in turn, the cavitation resistance. On the other hand, if the temperature of the substrate is too high, then, the coating performance deteriorates due to surface oxidation.

2.4. Cathode Arc Plasma Coating

Cathodic arc plasma deposition has been used extensively in the coating industries to deposit anticorrosion layers [70]. One such anti-corrosion coating that has gained widespread popularity and applications is chromium nitride (CrN) produced by numerous deposition methods reported in recent publications [71]. In Ref. [72], the cavitation resistance of the various assemblies of CrN, electroplated Cr and AISI 4140 (wt. %: 0.39 C, 0.24 Si, 0.71 Mn, 0.029 P, 0.04 Ni, 0.18 Mo and 1.06 Cr) were performed to reduce the risk of the CE that may occur on rotors of pumps, valves, impellers, ultra-sonic agitators, cooling system, etc., which are used extensively in hydraulic power plants. The CrN coatings were deposited by the cathode arc plasma deposition (CAPD) with and without an intermediate layer of the electroplated hard chrome, i.e., CrN-AISI 4140 and CrN-Cr-AISI 4140. The interlayer of Cr was deposited by the commercial electroplating (6 µm). The CAPD technique was used to deposit the CrN coatings (1.2 µm). The CE behaviour of the CrN coatings on AISI 4140 steel was investigated in freshwater. The CE tests were performed using the ultrasonic vibration system according to the ASTM G32-85 standard.

Figure 13 shows the cumulative weight loss of the samples as a function of the increasing cavitation time. The uncoated AISI 4140 sample shows the highest weight loss. The weight loss of Cr/AISI 4140, CrN/



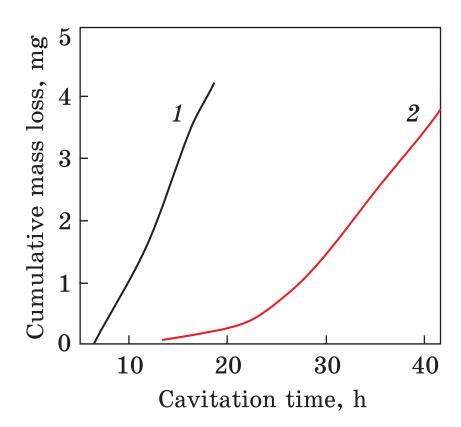


Fig. 13. Cumulative weight loss as a function of the cavitation time for AISI 4140 (1), Cr/AISI 4140 (2), CrN/AISI 4140 (3), and CrN/Cr/AISI 4140 (4) [72]

Fig. 14. Cumulative mass loss of the AISI 420 steel as a function of CE testing time for untreated (1) and carburized (2) samples [73]

AISI 4140 and CrN/Cr/AISI 4140 samples after 50 min was only one-third that of the uncoated AISI 4140 steel. Thus, the cavitation resistance of the coated samples is significantly improved in freshwater. At the same time, the weight loss magnitudes of the studied coatings make the following descending sequence: Cr/AISI 4140 > CrN/AISI 4140 > CrN/Cr/AISI 4140.

Another plasma coating method was studied in Ref. [73]. That study aimed to investigate the application of the low-temperature plasma carburization of the AISI 420 martensitic stainless steel with the composition (in wt.%): 0.305 C, 0.33 Si, 0.33 Mn, 0.019 P, 0.005 S, 12.21 Cr, 0.38 Ni, 0.025 Mo, 0.077 Cu, 0.006 Al, 0.043 V, 0.008 Nb, and Fe balance). The carburization process was performed on the as-hardened (non-tempered) samples, which were air-cooled from 1050 °C after a 0.5 h treatment at the austenization temperature. The plasma carburization was carried out for 12 h at 450 °C using a gas mixture of 99.5% (80% $\rm H_2 + 20\%~Ar) + 0.5\%~CH_4$ (in vol.%) at a pressure of 400 Pa. The total gas mixture flow rate was fixed at $1.67 \cdot 10^{-6}~\rm m^3 \cdot s^{-1}$.

Indirect CE tests were performed by the ASTM G32-10 standard using the 20 kHz ultrasonic vibratory equipment with a peak-to-peak displacement amplitude of 50 µm. Incubation period (IP), nominal IP (NIP), average erosion rate (AER), and maximum erosion rate (MER) were analysed. To obtain the dependence of the cumulative mass loss (CML) on the exposure time, the cavitation test was carried out until the erosion rate reached the MER value. Figure 14 shows the CML as the cavitation-erosion time function for the untreated and carburized surfaces. As seen, the NIP of the carburized surface is approximately three times higher than that of the untreated surface, *i.e.*, 7.8 and 23 h for the untreated and carburized samples, respectively.

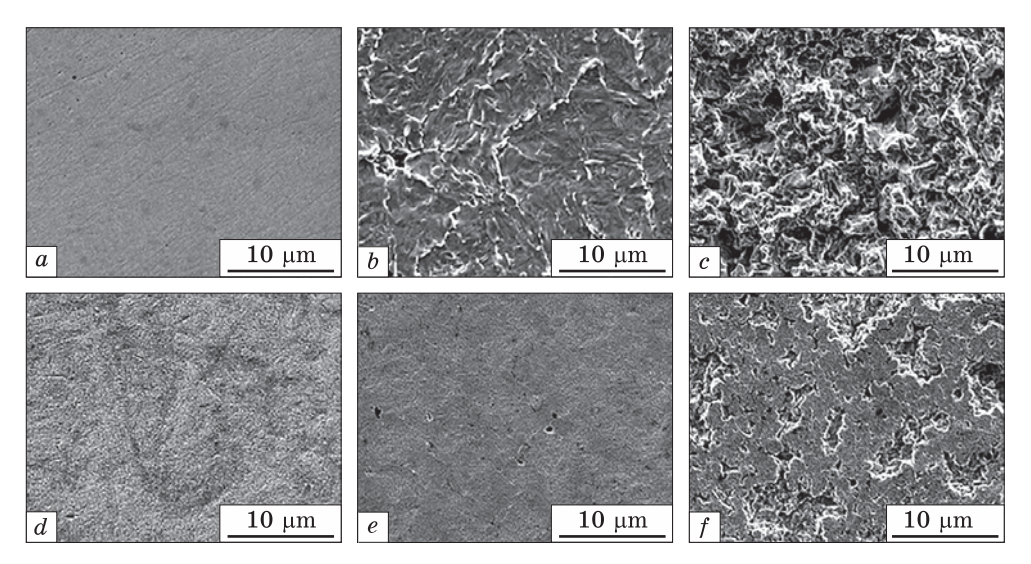


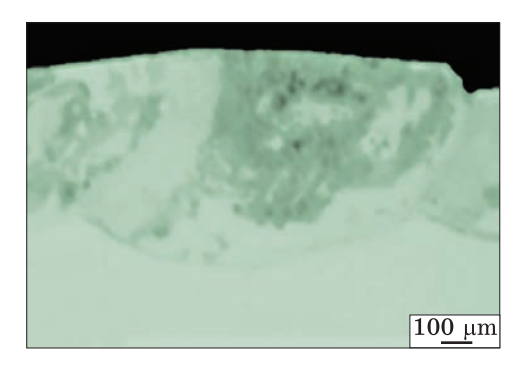
Fig. 15. SEM images of the as-polished (a-c) and as-carburized (d-f) samples in the initial state (a, d), after the CE tests for 4 h (b, e), 18 h (c), and 19.7 h (f) [73]

The surface morphologies are illustrated in Fig. 15, b, e, which respectively present the surfaces of the untreated and carburized samples subjected to 4 h of CE tests. For the untreated sample (Fig. 15, b), the intense plastic deformation occurs along the interfacial boundaries between the martensite (predominantly lath-type) grains and parent austenite grains. Material flows, thereby, causing the accumulation of the strained mass at the imperfections and protruding lips on the surface. The relatively intense plastic deformation (Fig. 15, b) is evident when comparing the untreated surface with the initial as-polished surface (Fig. 15, a). Note that the work-hardening effect due to the plastic deformation precedes crack formation, resulting in an effective mass loss in the untreated sample after an IP of 6 h, which agrees well with its relatively high surface hardness (approx. 8 GPa).

2.5. The Laser Surface Alloying

In work [74], the FeCoCrAlNiTi $_x$ (x—molar ratio; x = 0.5, 1.0, 1.5 and 2.0) high-entropy alloy coatings were prepared on 304 stainless steel by laser surface alloying. Accompanying the increase in hardness, the alloy for x = 2.0 exhibited the best CE resistance among the tested samples in distilled water. This is mainly due to the uniformly distributed hard intermetallic phases ${\rm Ti}_2{\rm Ni}$ and NiAl, which have a better ability to bear deformation and exhibit higher fracture resistance.

The study [75] aims for laser alloying of the surface on AISI 316 stainless steel using fine WC powder to improve the CE resistance. Fine WC powder of approx. 1 mm in size was employed as a convenient source of



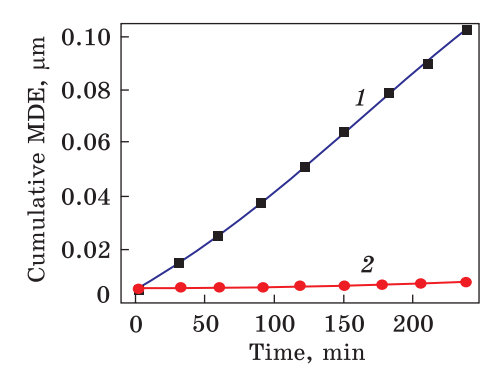


Fig. 16. Cross-sectional views of the laser surface-alloyed samples WC-316-2 [75] Fig. 17. Cumulative MDE as a function of the exposure time for AISI 316 steel (1) and coating (2) [75]

tungsten and carbon in the laser surface alloying of AISI 316 stainless steel for improving the CE resistance. Slurry containing WC powder was pre-placed on the substrate by pasting and then processed using the highpower 2.5 kW CW Nd:YAG laser to achieve surface alloying. Laser surfacing was achieved by parallel tracks with 50% overlap. Laser processing parameters and sample designations: laser power (kW) of 1.50-2.10, scanning speed (mm/s) of 25-35, spot diameter (mm) of 4, fluence (J/mm²) of 12.0-15.0, Ar as the shielding gas. CE tests were performed using an ultrasonic vibratory facility conforming to ASTM Standard ASTM G32-92. The peak-to-peak amplitude and the vibration frequency were 100 µm and 20 kHz. The cavitation liquid was 3.5% NaCl solution kept at 23 °C. The MER was calculated at the end of the test period, i.e., 240 min, and the reciprocal of MER was taken to be the CE resistance $R_{\rm a}$. As-received AISI 316 stainless steel (designated in this paper as As-316), with composition in wt.%: 18% Cr, 14% Ni, 3% Mo, 2% Mn, 1% Si, 0.08% C, 0.045% P, 0.03% S, and balance Fe was used. The slurry was prepared by mixing fine WC powder (particle size of @ 1 µm) and the binder (4 wt.% polyvinyl alcohol (PVA)). The average thickness of the alloyed layer for different samples was given as 0.35-0.60 mm.

With the suitable choice of processing parameters, the uniform alloyed layer free of cracks and pores was obtained, as shown in the optical micrograph of the sample WC-316-2 in Fig. 16 (laser parameters: laser power of 1.75 kW, scanning speed of 20 mm/s, spot diameter of 4 mm, fluence of 22.0 J/mm^2 , overlapping of 50%).

The XRD data show that the laser treatment results in the dissolution of fine WC powder in the melt pool. Then, they resolidified to form different types of complex metal carbides $M_{23}C_6$, M_7C_3 , M_6C ($M={\rm Fe,~W,~Cr}$), and tungsten carbides WC and W₂C, together with the g-FeCrNiW phase. Owing to the presence of the carbides, the microhardness HV of the al-

loyed layer is significantly increased from 200 HV for as-received AISI 316 to $\approx 1000 \ HV$ for the laser-treated samples.

The cumulative MDE as a function of the time for various samples in the CE test is given in Fig. 17, *a*. The best value of the CE resistance was obtained for the sample WC-316-2 (relative to

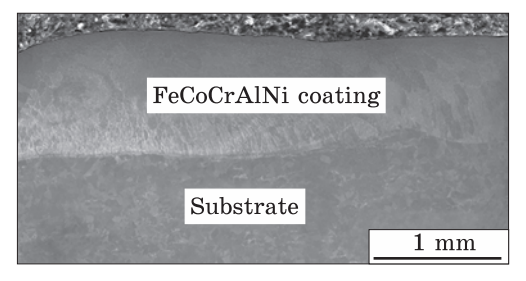


Fig. 18. Cross section of the FeCoCrAlNi HEA coating at low magnification [76]

AISI 316). The high cavitation erosion resistance of the laser surface-alloyed samples could be attributed to the microstructure composed of the carbide dendrites and interdendritic carbide/g-FeCrNiW eutectic.

The authors [76] have selected the high-entropy alloy (HEA) system FeCoCrAlNi with equiatomic ratios of Co, Cr, Al, and Ni powders as the CE-resistant coating on AISI 304 stainless steel using laser surface alloying. This treatment was carried out using the DL-HLT5000B-type continuous-wave CO₂ laser. The following laser parameters were selected: laser power of 2 kW, laser spot diameter of 3 mm, scanning speed of 3-7 mm·s⁻¹, and high purity argon gas at the flow rate of 15 L min⁻¹ was used as the shielding gas to prevent oxidation. CE tests were carried out using the ultrasonic-induced cavitation facility (HN-500M) conforming to the ASTM Standard G32-92 using the 3.5% NaCl solution at 23 °C. The frequency and the peak-to-peak amplitude were of 20 kHz and 60 µm, respectively. The sample was weighed at regular intervals. Then, the weight loss was converted to MDE and MDER at the end of the test period. The reciprocal of MDER was taken to be the CE resistance R_e. According to the XRD patterns, the FeCoCrAlNi HEA laser coating exhibits the single b.c.c. solidsolution phase. Figure 18 shows the cross-sectional SEM micrograph of the FeCoCrAlNi HEA coating at low magnification. It is evident from Fig. 18 that the HEA coating has an average thickness of 600 μm, being dense and uniform with little holes, cracks or other defects. A good metallurgical bonding between the coating and the substrate can be observed.

The cumulative MDE as the time function for various samples in the CE test is given in Fig. 19, a and the corresponding $R_{\rm e}$ is shown in Fig. 19, b. As a fact, $R_{\rm e}$ is increased for the coating, reaching 7.6 times in comparison with that of AISI 304 steel substrate. It can be concluded that the whole process of CE is divided into two stages. In the first stage of 5 h for the steel, the MDE increases slowly, indicating that little material is removed. At the second cavitation stage, the linear increase of MDE with the test time begins. At the end of the test, the cumulative MDE of AISI 304 steel substrate has reached 25.3 μ m. On the contrary, no observable cumulative MDE is recorded for FeCoCrAlNi HEA coating in the 5-hours test, implying that the coating is still within the incubation peri-

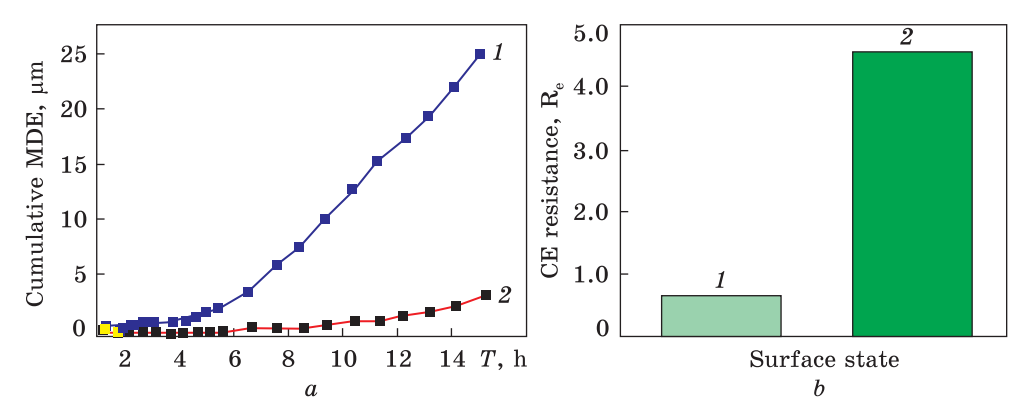


Fig. 19. Cumulative MDE as a function of the cavitation time (a) and the CE resistance R_e (b) for AISI 304 steel (1) and HEA coating (2) after the cavitation erosion test in 3.5% NaCl solution [76]

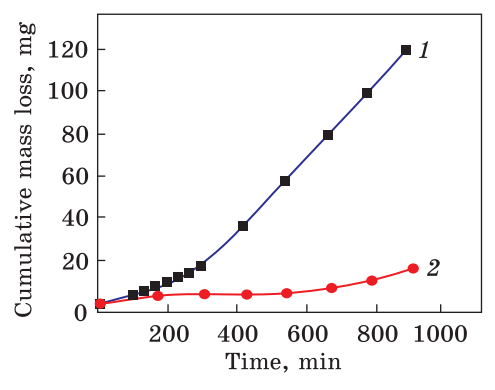
od. Then, the cumulative MDE of the HEA coating increases at an extremely slow rate and reaches only 3.5 µm at the end of 15 h, about 1/8 that of the AISI 304 steel substrate. Thus, the CE resistance coating is 7.6 times that of the AISI 304 stainless steel. The increase in cavitation erosion resistance could be attributed to the proper combination of hardness and toughness, which would contribute to the high CE resistance to the intense cavitation pulses. The microhardness of the HEA coating is more than 5 GPa, which is 2 times larger than that of such steel. The effects of laser treatment on improving CE are also described in the works [77, 78].

2.6. Nitriding Methods

Nitriding is a special hardening process that introduces nitrogen into the outermost surface of the metal parts and components [79–81]. Recent studies have found that nitriding provides the best CE resistance. Below, there are examples of several works in this direction, which report on using plasma, chemical-thermal and laser nitriding technologies.

In work [82], the low-temperature plasma nitriding of ASTM A 743 grade CA-6NM martensitic stainless steel was performed. The average chemical composition of the start material used in the study was 0.032% C, 0.63% Mn, 0.52% Si, 12.25% Cr, 4.42% Ni, 0.43% Mo, 0.024% P, 0.015% S, and Fe balance (wt.%). This material is typically applied for the manufacturing of hydraulic pumps and turbine rotors.

The gas mixture of N_2 and H_2 was adjusted by the mass flow controllers of $8.33\cdot 10^6~\rm m^3\cdot s^{-1}$ operating at the full scale, respectively. The pressure in the vacuum chamber was adjusted with the manual valve and measured with the capacitance manometer of $13.3\cdot 10^3~\rm Pa$ (100 Torr) in the full-scale operation. The cathode was negatively biased at a voltage of 660 V using a square form pulsed power supply. To ensure a stable dis-



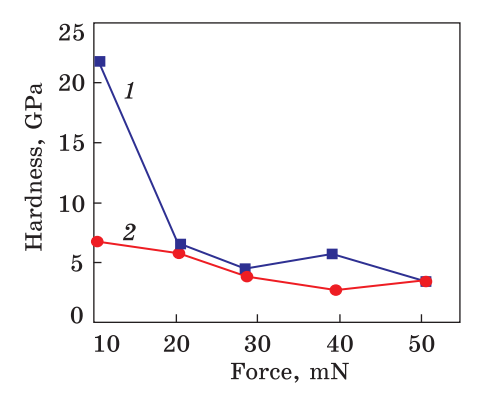


Fig. 20. Cumulative mass loss of CA-6NM martensitic stainless steel as a function of the CE time for the non-nitrided (1) and nitrided (2) samples tested for 12 h [82]

Fig. 21. The effects of the applied treatments on the hardness of nitride (1) and nitrided and annealed (2) samples of Ti-6Al-4V alloy [83]

charge, the electrical resistance was connected in series between the power supply and the discharge chamber. The nitriding process was carried out at 623 K for three different nitriding times of 6, 12 and 24 h, at a pressure of 532 Pa. The gas mixture was 5% $N_2 + 95\%$ H_2 , with a gas flow of $5 \cdot 10^{-6} \,\mathrm{m}^3 \cdot \mathrm{s}^{-1}$. Finally, the evolution of the surface nitrided layer thickness as a function of the nitriding time was in the diapason 3.9-9.2 µm. Such thickness evolution as a function of the nitriding time tends to be characteristic of the diffusion-controlled process. The steel in its start condition as non-nitrided presents two phases, the α -Fe (b.c.c.) and γ -Fe (f.c.c.), corresponding to tempered martensite and austenite (usually termed as retained austenite), respectively. XRD indicated the formation of the nitrogen-expanded martensite (α -N-Fe) and austenite (γ -N-Fe), respectively and the eventual presence of ϵ -Fe₂₋₃N (Fe₂₄N₁₀, hexagonal) Fe nitride. All these aspects point directly to the formation of the nitrogen-expanded austenite in the nitrided layer. The high surface hardness on the order of 16-18 GPa on average, obtained to the indentation depth of 100 nm, confirms the strengthening effect of the nitrogen in the investigated steels. In the selected indentation depth (1000 nm), the hardness increment of the nitrided surfaces was verified to be ≈ 2.5 times higher than that of the initial non-nitrided material. The CE tests were investigated employing the 20 kHz ultrasonic vibrator at peak-to-peak amplitude of 50 µm. The cumulative mass loss (CML) as a function of the CE testing time up to 900 min (15 h) is presented for the studied samples in Fig. 20. Evidently, the CE resistance of the CA-6NM steel low-temperature plasma nitrided samples is strongly increased concerning the material in its start condition as non-nitrided. It is also observed that the steel CE effect is directly related to the nitriding time. If the nitriding time is longer, the CE resist-

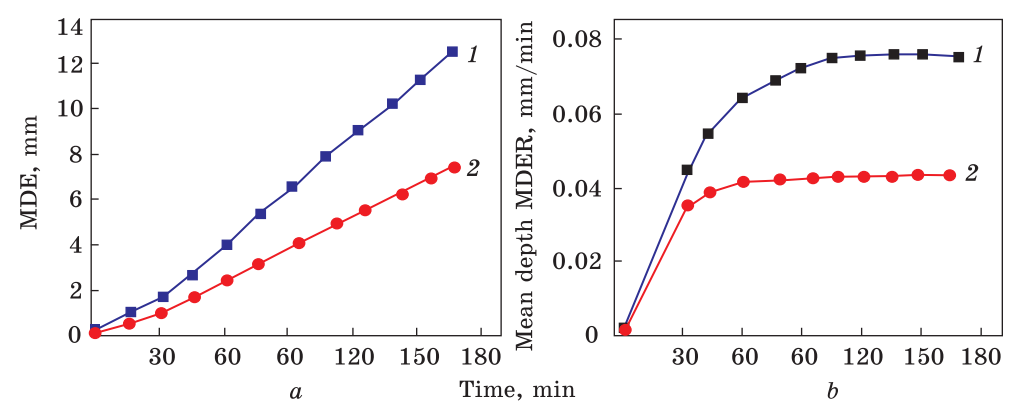
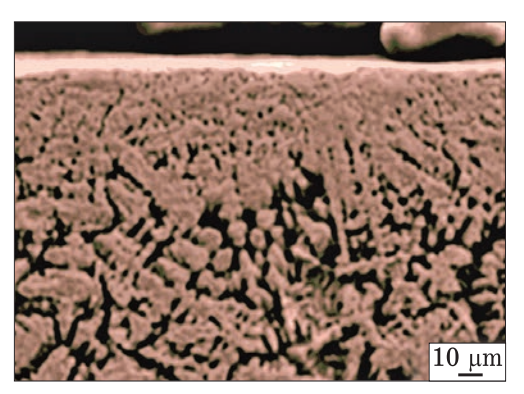


Fig. 22. The effects of the applied treatments on the CE resistance of Ti-6Al-4V alloy in the annealed (1), and nitrided (2) states: MDE (a) and MDER (b) as the functions of the cavitation time [83]

ance of the treated steel is higher. Thus, the present work reports the CE resistance increase for low-temperature plasma nitrided CA-6NM martensitic stainless steel.

The work in the paper [83] aims to identify the contribution of gas nitriding on ultrasonic CE of the Ti-6Al-4V alloy. Owing to good mechanical and corrosion resistance properties, this material was selected to fabricate the components for aircraft, marine, power generation or biomedical fields. The chemical-thermal nitriding was performed in the flow of 5 h^{-1} nitrogen (grade 4.8 and 99.9998% purity) and 2 h^{-1} NH₃ (grade 3.8, with $NH_3 > 99.98\%$, $H_2O < 200$ ppm, oil < 10 ppm). One set of the samples was further annealed at 700 °C for 240 min, to increase the nitrogen diffusion in the surface layers. The cavitation tests were made according to ASTM G32-2010 standards, using ultrasonic vibratory equipment with 20 kHz vibration frequency and 50 µm peak-to-peak amplitude, by immersion in tap water at a constant temperature (23 °C). Involving the interface reactions between the gas and the alloy as the result of the gas nitriding process, the TiN or Ti₂N layers were formed on the sample surface. The hardness of the nitrided samples appears higher than the one of the additionally heat-treated samples (Fig. 21). The mean depth of erosion (MDE) data detailed in Fig. 22, a indicates the significantly improved effects of the nitrided samples, compared to the sample after nitriding followed by heat treatment. At the same time, both nitrided samples had a substantially better cavitation resistance than the annealed Ti-6Al-4V sample tested under the same conditions. The MDER parameter demonstrates similar behaviour (Fig. 22, b).

As an example of the laser gas-nitriding study for improving the cavitation resistance, we present the work [84]. In this work, the continuous wave 2 kW Nd-YAG laser was used for the nitriding process under the



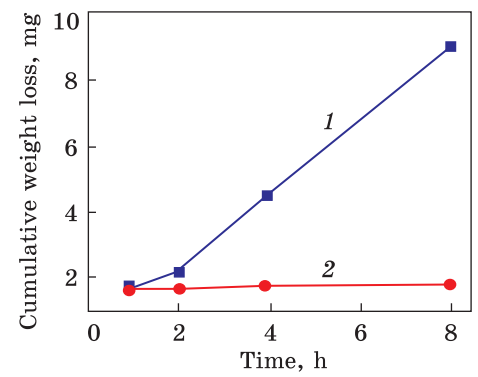


Fig. 23. Cross-sectional microstructure after laser nitriding Ti [84]

Fig. 24. Relationship between the cumulative weight loss and CE time for as-received (1) and laser nitrided (2) Ti-6Al-4V alloy surfaces [84]

pure nitrogen environment on the titanium and Ti-6Al-4V alloy surfaces. Under the conditions of this study, the optimum set of laser power, beam diameter, scanning speed and gas flow rate was found to be 500 W, 2 mm, 5 mm/s, and 60 °C/min, respectively and 50% tracks' overlapping rate. The cavitation tests were induced by longitudinal oscillation at 20 kHz with the peak-to-peak amplitude of 50 μ m in 3.5% NaCl solution at 23 °C.

After nitriding, the Ti surface became relatively flat and coloured in a golden yellow. XRD analysis reveals both the cubic TiN and hexagonal Ti phases. Figure 23 shows the cross-sectional microstructure of the nitrided Ti. The microstructure of this surface layer is mainly composed of the TiN dendrites. Good metallurgical bonding was demonstrated at the interface between the nitride layer and the substrate alloy.

Figure 24 shows the relationship between the cumulative weight loss of all tested samples and the CE time. As seen, the cumulative weight loss of all tested samples increases with the development of the cavitation time. In addition, the laser gas nitrided Ti and Ti–6Al–4V samples exhibit excellent $R_{\rm e}$ in comparison with the mechanically polished (MP) samples. The weight loss of the nitrided samples is only about 0.90 mg, even after a CE time of 8 h. The $R_{\rm e}$ and its normalized values for the various test samples can be positioned in the following descending row: laser gas nitrided > MP Ti6Al4V > MP Ti. As a result, the $R_{\rm e}$ magnitudes for the MP Ti and the MP Ti–6Al–4V samples were improved using laser processing by 13.06 and 9.42 times, respectively. The increase in the microhardness of the eroded Ti and Ti–6Al–4V samples was of 56.8% and 17.0%, respectively.

3. Surface Treatment Methods

3.1. Laser Surface Melting

Laser surface treatment to achieve melting, alloying, or cladding is an attractive and promising method of metal surface modification. Laser surface melting (LSM) is a simple method for surface modification, which enhances the surface properties via homogenization and refinement of the microstructure [85-87]. In Ref. [88], LSM was used to improve the CE resistance of the manganese-nickel-aluminium bronze (MAB), which is widely widespread in manufacturing large marine propellers. Chemical composition of this alloy (wt.%): Cu 75.6, Mn 10.8, Al 7.8, Fe 3.6, Ni 2.2. Before LSM, the samples were sandblasted to reduce the reflectivity of the laser beam. LSM was carried out using the 2 kW CW Nd:YAG laser. Argon flowing at 10 min⁻¹ was used as the shielding gas. The surface melting was achieved owing to a 50%-overlap between the melt track parallel to adjacent tracks. The CE test was carried out in a 3.5 wt.% NaCl solution at 23 °C using the ultrasonic vibratory facility conforming to the ASTM Standard G32-92, the peak-to-peak amplitude and vibration frequency of 100 µm and 20 kHz, respectively.

The as-received MAB consists of a dark k-phase (intermetallic phase) embedded in the matrix comprising α - and β -phases. Under the laser irradiation, the thin layer of the sample surface melted and then rapidly solidified by self-quenching. Results of preliminary trials on the laser parameters show that when the laser fluence is too low ($<3 \text{ J/mm}^2$), some k-phase remains unmelted, and the microstructure is not homogeneous. However, if the fluence is too high ($>200 \text{ J/mm}^2$), the grains in the melt layer are heavily twinned. For the samples laser-treated with fluence in the range selected in the present study, the microstructure of the melt layer is homogeneous and refined. It consists of the single β -phase (Fig. 25), in contrast to the complex and heterogeneous microstructure of

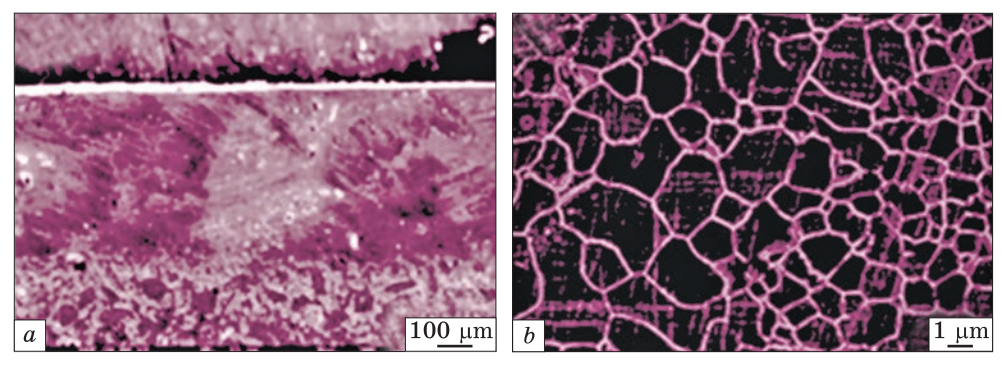
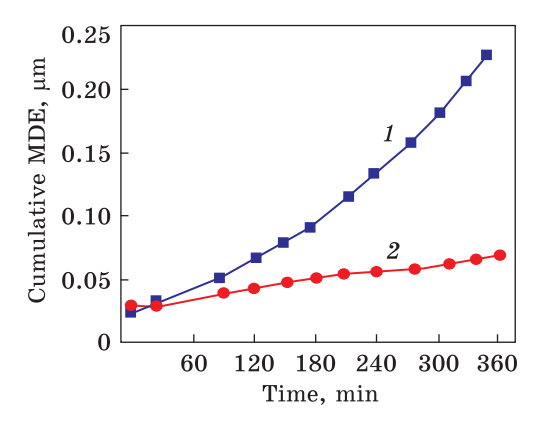


Fig. 25. SEM micrographs of MAB-2-35 showing (a) cross-sectional view of melt pool, and (b) homogenized and fine-grained microstructure [88]

Fig. 26. Cumulative mean depth of erosion (MDE) as a function of the exposure time for as-received (1) and laser melted (2) MAB [88]

the as-received MAB. The grain size in the melted layer is of the order of a few micrometres, which is much smaller than that in the as-received alloy.

The best MDE value is shown in Fig. 26 for the as-received MAB produced at the following laser



parameters: laser power of 1000 W, spot diameter of 2 mm, scanning speed of 35 mm/s, fluence of 14.29 J/mm². The curve for the as-received NAB has also been included for comparison. LSM of MAB has resulted in the erosion resistance increase by a factor ranging from 3.9 to 5.8 times. Such an increase is attributable to the β -phase, which has a higher hardness than the α -phase, and grain refinement. It was concluded that for the as-received MAB, CE was initiated at the k-phase and the α/β -interface, and propagated in the matrix. For laser-treated MAB, erosion started at some triple junctions and propagated along the grain boundaries.

3.2. Friction-Stir Processing

Friction-stir processing (FSP) is a solid-state surface modification technique, which is based on principles of friction-stir welding, and can be used to repair and improve the quality of the local areas, such as strength (and consequently the overall performance of the metal product). In this method, the rotating tool plunges into the surface to be modified and then travels along the surface. During FSP, material locally undergoes severe plastic deformation at elevated temperatures caused by frictional and plastic deformation-induced heat. As a result, the refined or ultrafine-grained microstructure is formed due to dynamic recrystallization [89, 90]. It was found that friction stir welded joints show remarkable fatigue life and fatigue crack growth resistance compared with those of base materials [91]. Owing to the cyclic nature of the cavity collapse, the CE damage is usually considered a fatigue-like process. Therefore, it appears that FSP can provide good CE resistance for the metal alloys.

Among structural materials, stainless steels, especially, of austenitic grades (e.g., AISI 304L and AISI 316L), are of particular practical importance in the hydraulic components exposed to CE. The aim of the study [92] was to improve the CE erosion resistance of AISI 316L stainless steels using FSP to help evaluate the feasibility of repairing and strengthening local areas in hydraulic machinery. The chemical composition of the

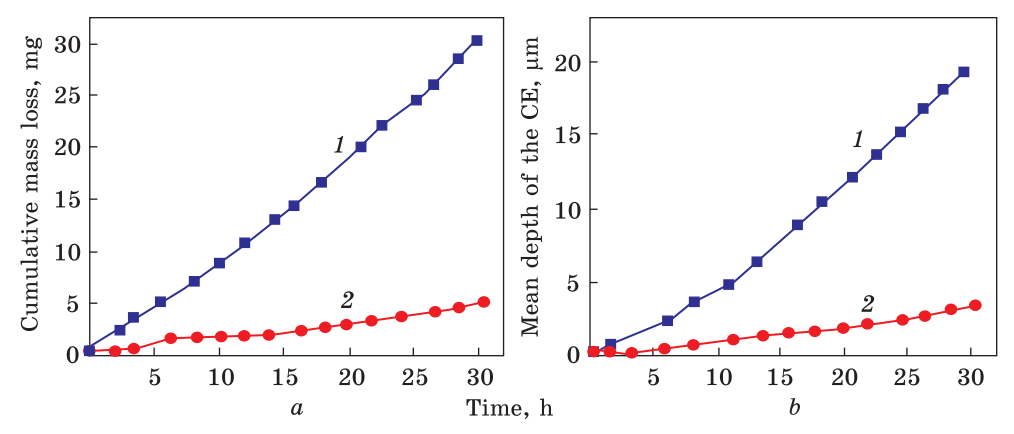


Fig. 27. Cumulative mass loss (a) and mean depth (b) characterizing the CE as a time function for as-received (1) and FSP 200-30 (2) AISI 316L steel samples [92]

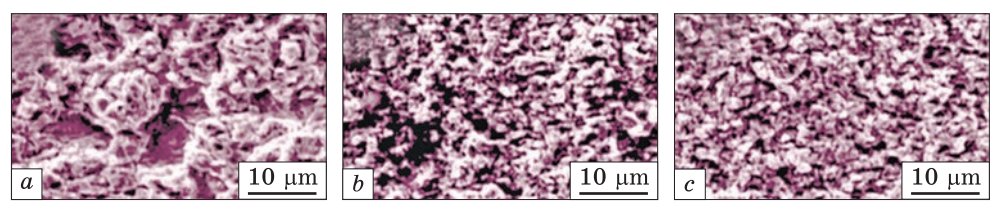


Fig. 28. SEM micrographs of the eroded surfaces for the as-received material (a) and FSP-treated samples in 315-30 (b) and 200-30 (c) regimes after the CE test for 30 h [92]

AISI 316L stainless steel (wt.%): C—0.026, Cr—16.5, Ni—10.0, Mo—2.0, Mn—0.86, Co—03.36, Cu—0.22, Si—0.27, P—0.029, S < 0.003, Al—0.003, Fe—balance. Before FSP, the samples were annealed to an austenitic structure. The WC-based tool with a shoulder diameter of 16 mm, pin length of 0.5 mm, and pin diameter of 5 mm was used in the FSP procedure. To obtain the different grain sizes in the sample structure, the single-pass FSP was carried out at a constant traverse speed of 30 mm/min and two different rotation speeds of 200 (sample 200-30) and 315 rpm (sample 315-30). The CE tests were performed using a vibratory oscillator operating at 20 kHz frequency and 50-µm peak-to-peak amplitude, according to the ASTM-G32 in the distilled water at 25 °C. The CE test of each sample was performed for 30 hours.

The average grain size of the base material is initially 14.8 μ m, which is reduced to 4.6 and 1.7 μ m at the surface of FSP samples 315-30 and 200-30, respectively. It is the result of severe plastic deformation during FSP. The XRD patterns of the base material and FSP samples show that the phase microstructure of the steel samples does not change and remains fully austenitic even after severe plastic deformation. The cumulative mass loss and mean depth of erosion as a function of the exposure time are shown in Fig. 27 for the as received and after the FSP samples. It is observed that FSP has a remarkable effect on the CE resistance of AISI 316L

stainless steel. In addition, the FSP samples significantly exhibit lower mass loss over the whole cavitation test. The incubation times, during which material loss is negligible, are approximately 0.5, 3 and 5 hours for the as-received, 315-30 and 200-30 samples, respectively. Figure 28 shows the surface morphology of the steel samples after the CE tests. The eroded surface of the as-received material demonstrates the large and deep erosion craters, while shallow pits were observed after the FSP. As observed, the depth of the waviness in the surface of the 200-30 sample having the smaller grain size is lower than that of the sample 315-30. Additionally, the appearance of the eroded surface of the FSP samples looks to be more homogeneous than the as-received material. The average hardness of the FSP samples is of 327 HV and 384 HV for 315-30 and 200-30, respectively. Therefore, the surface of the FSP samples is nearly twice as hard as the as-received material.

Nickel aluminium bronze (NAB) is a copper alloy of high strength, corrosion and erosion resistance. NAB consists of Al, Fe, Ni and Mn as the alloying elements, which have high strength and erosion resistance [93, 94]. The combination of high strength and erosion resistance makes the NAB to be a suitable material for marine and shipbuilding applications. The failure of the marine system is still mainly attributed to seawater corrosion and CE. Studies on the CE behaviour of the NAB alloys suggest that the microstructure of NAB alloys influences the cavitation erosion behaviour [95]. During cavitation, microcracks tend to propagate in the α -phase, and the favourable nucleation sites are adjacent to $\kappa_{\rm III}$ and $\kappa_{\rm IV}$ precipitates [95–97]. The studies of the cavitation corrosion behaviour of the NAB alloys concluded that the selective phase corrosion and cavitation-induced stresses caused the micro-cracks propagation during cavitation. The study [97] provided the basis for improving the CE resistance of

Table 3. The FSP parameters and response for the experimental design results [97]

Run tool rotational speed, RPM	Tool traverse speed, mm/min	Tool Shoulder diameter r, mm	Grain Size, μm	Ultimate tensile strength, MPa	Corrosion rate, MPY	Mass loss due to cavitation, $\mathrm{gm}\cdot 10^{-3}$
931	30	20	16.21	608.26	10.05	0.56
931	30	18	14.82	661.09	3.73	0.49
1216	40	20	17.14	644.03	7.18	0.76
1216	40	18	17.72	620.92	4.79	4.5
1216	30	20	18.50	612.28	4.56	2.09
1216	30	18	19.60	594.45	6.22	5.95
931	40	20	20.04	560.096	8.80	7.50
931	40	18	19.66	625.37	7.52	6.86
as-cast			190.15	661.09	36.05	38

NAB alloys using the FSP. In this work, the effects of the process parameters on the cavitation and corrosion behaviour of the FSP-ed NAB alloys were investigated. Chemical composition of NAB alloy (wt.%): Cu 80.5, Al 9.6, Fe 3.6, Mn 1.5, Ni 4.8. The FSP process parameters, such as tool rotation, traverse speed, and shoulder diameter, were used (Table 3). CE testing for 4 hours of the as-cast and FSP-ed NAB surfaces was assessed using the ultrasonic vibratory testing rig as per ASTM G 32-92 standards in 3.5% NaCl solution. The microstructure of the as-cast NAB alloy comprises the coarse Cu-rich f.c.c. α -phases, β -phases and fine k-phase particles. FSP causes the breaking of the coarser α - and β -phases and homogenization of k-phases due to the severe plastic deformation. The micrographs suggest that the FSP-ed surface consists of fine globular α -phases along with some elongated banded morphology α -phases. The results obtained for the grain size are listed in Table 3, and the grain size varied in the range of 14.82 to 20.04 µm for the FSP-ed conditions, which was found to be 190.15 µm for the as-cast condition. The effects of the input process parameters of FSP on average grain size, ultimate tensile strength (UTS), corrosion rate and mass loss due to cavitation are shown in Table 3. The authors of Ref. [97] made the following conclusions based on the results of the experiment. The cavitation resulted in a rougher surface containing pits and cracks. The as-cast sample underwent higher surface and subsurface damage compared to the FSP-ed surface, which is attributed to the homogenous and fine-grained structure with enhanced mechanical properties. The hardening capacity, grain size, and strain-hardening exponent are the significant parameters correlated with the mass loss in regression.

3.3. Tungsten Inert Gas Welding

Tungsten inert gas (TIG) welding or dressing is the process in which an arc is formed between the non-consumable tungsten electrode and the work piece to join the metals together. The shielding gas is used to protect the weld from atmospheric contaminants that could cause weld defects such as porosity. The TIG process, known for its ability to produce high-quality welds and coatings, allows for precise control over the microstructural characteristics of the deposited alloy [98–101]. Currently, TIG welding/dressing procedures are mostly used in the aerospace industry for producing structural parts with high requirements for welding joints because of their high quality, efficiency, and flexibility. Below, there are given typical examples of the successful application of TIG for the enhancement of the CE resistance of metallic materials.

For example, the authors of Ref. [102] applied TIG method to improve the CE resistance of the nodular graphite cast iron. This material has an excellent casting capacity, good machinability, and a lower price compared to steel. It is of importance that due to the spherical shape of the graphite,

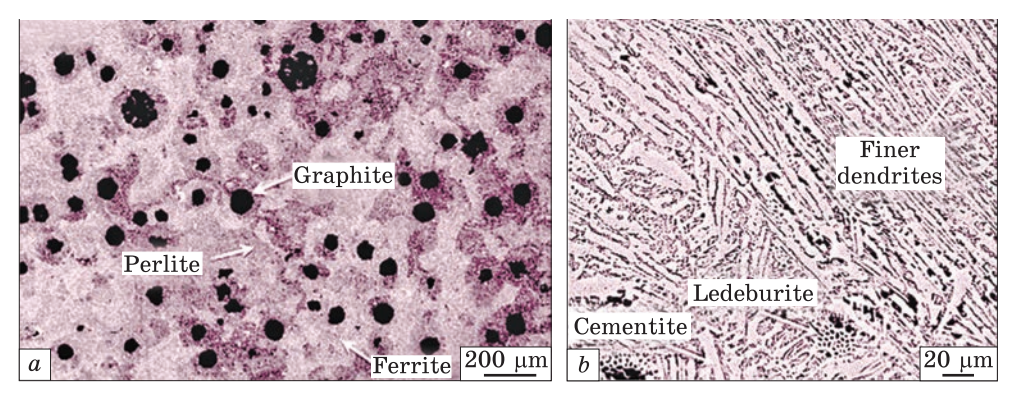


Fig. 29. SEM images of microstructure of the nodular graphite cast iron used in the experiments (a) and TIG remelted layer, using 60-A current (b) [102]

the tendency to propagate cracks is reduced, leading to mechanical strength and toughness characteristics comparable to the ones of the unalloyed steels with a similar structural matrix (ferrite and pearlite content). This alloy is used for manufacturing crankshafts for automotive engines, presses, and rolling mills, as well as pump and valve bodies [103–105]. The investigated material was the ferrite-pearlite matrix nodular cast iron with the following chemical composition (wt.%): C—3.57, Si—2.51, Mn—0.23, P—0.044, S—0.01, Fe—rest. According to Fig. 29, the base metal microstructure consists of approximately 60% ferrite and 40% pearlite. The TIG experiments were conducted using an electric arc voltage of 9.5 to 10 V with 10 cm/min welding speed, 1.5 mm as the distance between the electrode and the sample, and 3-mm scanning steps, for four values of the welding current: 60, 70, 80, and 90 A. The cavitation tests were conducted using the piezoceramic vibrating system according to the requirements of ASTM G32-2010.

TIG heating leads to the local melting of the sample surface, followed by rapid cooling (over 150 °C/min), and the primary crystallization process starts with the undercooling of the melt, when the temperature falls below the equilibrium coexistence of the liquid and solid phases. As a result of this treatment, the solidification occurs based on the metastable Fe–Fe₃C system. In the marginal layer, the white cast iron structure is formed instead of the one corresponding to the stable Fe–C system. Figure 29, b illustrates the fine microstructure of the marginal layers, made up of ledeburite eutectic, acicular cementite, dendritic transformed austenite, and traces of nodular graphite, undissolved during heating at the melting temperature. Increasing the current from 60 A to 90 A and the heat input from 3420 to 5400 J/cm results in a slight increase in the quantity of undissolved graphite nodules. The SEM images of the melted area processed at 60 and 90 A show that the cementite phase has a plate-like morphology with a thickness of 1 µm and a length of more than 10 µm.

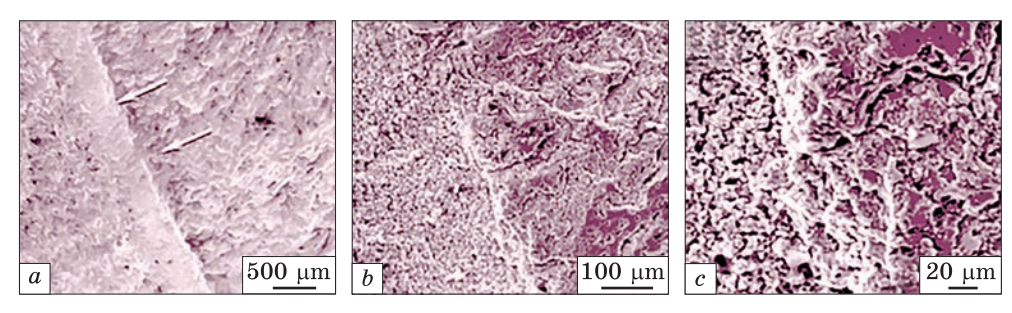


Fig. 30. SEM images at different magnifications of the 165 min cavitated surface for TIG re-melted sample of cast iron: $\times 150$ (a), $\times 500$ (b), and $\times 1500$ (c) [102]

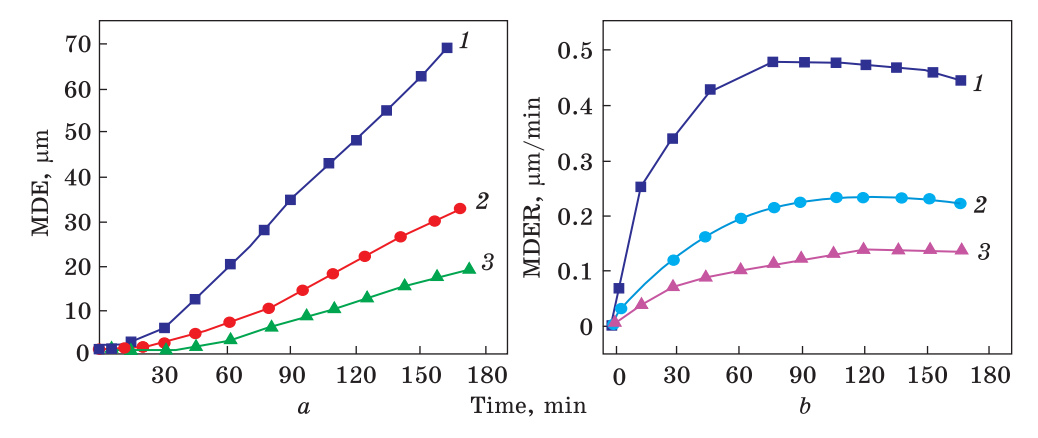


Fig. 31. Influence of the CE time on MDE (a) and MDER (b) for the stress-annealed (1), and surface TIG re-melted samples using 90-A (2) and 60-A (3) cur-rents [102]

The space between the eutectic plates is less than 0.5 µm. During the primary crystallization process, the adjacent graphite nodules (Fig. 29, a) transform to the fine and acicular eutectics consisting of the thin and long cementite (Fig. 29, b) and the transformed austenite plates. The topography of the cavitated samples after 165 min erosion revealed that smallerscale craters with depths of less than 1 µm are formed in TIG-melted (Fig. 30). Around the small craters, there is the work hardening due to the repeated impact of the cavitation bubbles. The material removal is due to the initiation of the fatigue cracks on the interface of the overlapping layers during remelting (Fig. 30). Figures 14 and 31, a, b highlights the MDE and the MDER dependencies as the function of the CE time. These characteristic curves for the 60 and 90 A currents are compared to those of the heat-treated nodular iron by stress annealing. The lowest values of MDE and MDER were obtained after TIG remelting using the current of 60 A with a heat input of 3420 J/cm. By comparing the values at the end of the cavitation tests (after 165 min) and according to ASTM G32-2010, the cavitation erosion resistance ($R_{cav} = 1/MDER$) is 7.3 for 60 A, 4.3 for 90 A, and 2.2 for the annealed state. By TIG remelting of the surface, an increase in CE of approx. 2 to 3 times was obtained, depending on the current used.

The experimental results of the CE test showed a significant improvement in the nodular cast iron resistance after the TIG remelting. Compared to the structural condition obtained from the stress relief annealing, the layers processed at the 60 A current show an increase of about three times for the CE resistance. For a higher 90-A current, the cavitation resistance increase is approximately two times. The remelting of the nodular cast iron via TIG, without the filler material, proved to be a simple and inexpensive way to produce hard surfaces with a unique microstructure and high cavitation resistance.

Additionally, work [106] compares the effects of the TIG process and stress-relieving annealing treatment on the degradation mechanism by CE of the grey cast iron with the microstructure consisting of the lamellar graphite incorporated in the pearlite matrix. As shown, TIG allows providing a double lower CE-induced mass loss and a triple lower erosion rate than those observed after heat treatment.

4. Summary and Conclusions

Cavitation is the highly complex surface process, in which the liquid static pressure falls below its vapour pressure, resulting in the formation of small vapour-filled bubbles in the liquid. Their appearance is the first event in this process. The second stage of cavitation includes the subsequent collapse or implosion of the vapour bubbles back to the liquid state when the local static pressure again becomes higher than the fluid vapour pressure. As vapour bubbles collapse near the material surface, they generate high-speed and high-energy liquid jets and localized shockwaves, which can cause the removal of the material from the surface, leading to the so-called 'cavitation erosion' (CE).

Understanding the CE mechanism and its potential for surface damage is crucial in designing and maintaining the metal systems and parts that involve the vibration fluid flow. The mass loss owing to the cavities formed during CE reduces the lifetime of the machine parts and/or equipment, which can cause a catastrophic collapse. The damage caused by the CE gradually extravagates in many industry fields, such as overflow components of the metallurgical, petrochemical, mineral mining and separation, water conservancy, transportation and deep-sea mining vehicles. As demonstrated, the CE is a general phenomenon in such fields as aviation, navigation, the hydraulic turbine of the hydropower station, the rudder blade or arm of the high-speed vessel, and the afterburner fuel pump of the aeroengine.

The special type of cavitation is ultrasonic cavitation. In this case, the CE induced by ultrasonic waves involves the transmission of the sound waves within the ultrasonic frequency spectrum, which equals or exceeds

20 kHz, through the liquid medium. The cavities (bubbles) in the liquid are formed and grow, when the negative pressure amplitude drops to or below the vapour pressure of the liquid. Subsequently, these bubbles collapse during the cycle of the positive pressure and generate high-pressure shockwaves and microjets. One of the most important applications of ultrasonic cavitation is the execution of the cavitation tests of the materials to provide a quantitative description of the relationship between the CE characteristics in the controlled environment and the material properties.

As a rule, the material resistance to the CE is presented graphically by the 'mass/volume loss vs. exposure time' curves or erosion rate during the exposure period in the controlled liquid medium. Such an erosion test is significantly more accelerated than the actual cavitation that affects the studied material in its operational life. This is due to either a much higher 'repetition rate' of the cavitation events, their higher energetic, more developed cavitation, or a combination of the above. Therefore, the ultrasonic cavitation test is a convenient and express predictive method for evaluating the cavitation resistance of materials. The CE resistance of the metal samples is usually tested by the typical ultrasonic vibration apparatus according to the ASTM G32-16 test standard. The most commonly used liquid medium is the tap water, the distilled water or the NaCl solution, which are kept at 18–25 °C. The vibration frequency of the ultrasonic horn is in the range of 20–40 kHz.

Among many studies devoted to the problem of cavitation, a special place is occupied by works devoted to methods of protection against this phenomenon that is harmful to technology. The present paper reviews the current development of surface treatments aimed at improving the CE resistance of the metallic parts working under vibration conditions in different liquid environments. This analysis allows for a better understanding of the role of the surface treatment methods and parameters on the structure and mechanical properties of the near-surface region, helping to enhance the protection against the destructive cavitation effects. The following methods of applying protective coatings are considered: microarc oxidation, arc spraying, high-velocity oxygen fuel deposition, cold spraying, cathode arc plasma spraying, laser surface alloying, and gas and plasma nitriding. Several high-energetic surface treatment methods, such as laser surface melting, friction stir processing, and tungsten inert gas (TIG) welding (dressing), are considered. Quantitative estimates of the improvement in CE resistance obtained using high-frequency cavitation tests are presented. The extent of the CE resistance of the analysed coatings is observed to be 6-to-30 times higher compared to untreated metal materials, including the alloys based on Fe, Cu, Ni, and Al.

Acknowledgement. This research was funded by the Ministry of Education and Science of Ukraine (state reg. No. 0124U001001) and the National Academy of Sciences of Ukraine (state reg. No. 0123U102368).

REFERENCES

- 1. C.E. Brennen, Cavitation and Bubble Dynamics (Cambridge University Press: 2013).
- 2. R.T. Knapp, J.W. Daily, and F.G. Hammitt, Cavitation (McGraw-Hill: 1970).
- 3. F.R. Young, Cavitation (Imperial College Press: 1999).
- K.S. Suslick, Science, 247: 1439 (1990); https://doi.org/10.1126/science.247.4949.143
- H. Crockett and J. Horowitz, J. Press. Vessel Technol., 132: 024501 (2010); https://doi.org/10.1115/1.4000509
- C. Kang, N. Mao, W. Zhang, and Y. Gu, Ann. Nucl. Energy., 110: 789 (2017); https://doi.org/10.1016/j.anucene.2017.07.028
- B.K. Sreedhar, S.K. Albert, and A.B. Pandit, Wear, 372–373: 177 (2017); https://doi.org/10.1016/j.wear.2016.12.009
- D.E. Zakrzewska and A.K. Krella, Adv. Mater. Sci., 19: 18 (2019); https://doi.org/10.2478/adms-2019-0019
- 9. A.K. Krella, Wear, 258: 604 (2005); https://doi.org/10.1016/j.wear.2004.11.025
- M. Dular and O. Coutier-Delgosha, Int. J. Numer. Meth. Fluids, 61: 1388 (2009); https://doi.org/10.1002/fld.2003
- G.Y. Gao, S.H. Guo, and D. Li, Materials, 17: 1007 (2024); https://doi.org/10.3390/ma17051007
- 12. K.H. Kim, G.L. Chahine, J.-P. Franc, and A. Karimi, *Advanced Experimental and Numerical Techniques for Cavitation Erosion Prediction* (Berlin: Springer: 2014).
- 13. A. Gedanken, *Ultrason. Sonochem.*, 11: 47–55 (2013); https://doi.org/10.1016/j.ultsonch.2004.01.037
- D. Leng, S. Shao, Y. Xie, H. Wang, and G. Liu, Ocean Eng., 228: 108565 (2021); https://doi.org/10.1016/j.oceaneng.2020.108565
- Y.-G. Ren, L. Yang, Y.-J. Liu, K.B. Yu, and J.H. Zhang, J. Marine Sci. Eng., 9: 682 (2021); https://doi.org/10.3390/jmse9060682
- S. Wu, Y. Wu, J. Tian, and H. Ouyang, Eng. Appl. Comput. Fluid Mech., 16: 1048 (2022); https://doi.org/10.1080/19942060.2022.2067243
- 17. R. Singh, S.K. Tiwari, and S.K. Mishra, J. Mater. Eng. Perform., 21: 1539 (2012); https://doi.org/10.1007/s11665-011-0051-9
- M. Brunhart, C. Soteriou, C. Daveau, M. Gavaises, P. Koukouvinis, and M. Winterbourn, *Wear*, 442: 203024 (2020); https://doi.org/10.1016/j.wear.2019.203024
- R. Khare and V. Prasad, Ocean Eng., 221: 108512 (2021); https://doi.org/10.1016/j.oceaneng.2020.108512
- C.K. Toh, Int. J. Adv. Manuf. Technol., 31: 688 (2007); https://doi.org/10.1007/s00170-005-0249-9
- H. Soyama and F. Takeo, J. Mater. Process. Technol., 227: 80 (2016); https://doi.org/10.1016/j.jmatprotec.2015.08.012
- M. Mathias, A. Göcke, and M. Pohl, Wear, 150: 11–20 (1991); https://doi.org/10.1016/0043-1648(91)90302-B
- Q.J. Peng, T.G. Ming, Y.L. Han, and T. Zhang, Surf. Coat. Technol., 496: 131675 (2025); https://doi.org/10.1016/j.surfcoat.2024.131675
- H. Soyama, K.L. Wong, D. Eakins, and A.M. Korsunsky, Int. J. Fatigue, 185: 108348 (2024);
 - https://doi.org/10.1016/j.ijfatigue.2024.108348

- H. Soyama, C. Kuji, and Y.L. Liao, J. Magnesium Alloys, 11: 1592 (2023); https://doi.org/10.1016/j.jma.2023.04.004
- 26. P. Murugesan, S.H. Jung, and H. Lee, *Mater. Design*, **229**: 111906 (2023); https://doi.org/10.1016/j.matdes.2023.111906
- 27. Y. Iwai, T. Honda, H. Yamaa, T. Matsumura, M. Larsson, and S. Hogmark, *Wear*, **251**: 861 (2001);
 - https://doi.org/10.1016/S0043-1648(01)00743-8
- 28. L.A. Espitia, H. Dong, X.Y. Li, C.E. Pinedo, and A.P. Tschiptschin, *Wear*, 332–333: 1070 (2015);
 - https://doi.org/10.1016/j.wear.2014.12.009
- 29. V. Schulze, F. Bleicher, P. Groche, Y.B. Guo, and Y.S. Pyun, *CIRP Ann.*, **65**: 809 (2016);
 - https://doi.org/10.1016/j.cirp.2016.05.005
- 30. C.E. Brennen, Cavitation and Bubble Dynamics (New York: Oxford University Press: 1995).
- 31. L.Z. Ye, X.J. Zhu, L.J. Wang, and C. Guo, *Ultrason. Sonochem.*, **40**: 988 (2018); https://doi.org/10.1016/j.ultsonch.2017.09.013
- 32. L. Ye and X. Zhu, Adv. Mech. Eng., 9: 1 (2017); https://doi.org/10.1177/1687814017712947
- 33. J. Doktycz and K. S. Suslick, *Science*, 247: 1067 (1990); https://doi.org/10.1126/science.2309118
- 34. T. Volkov-Husović, S. Martinović, A. Alil, M. Vlahović, B. Dimitrijević, I. Ivanić, and V. Pavkov, *J. Min. Metall. Sect. B-Metall.*, **60**: 295 (2024); https://doi.org/10.2298/JMMB240118018V
- 35. https://www.hielscher.com/information-about-ultrasonic-cavitation.htm
- 36. L.Q. Wang, N. Qiu, D.H. Hellmann, and X.W. Zhu, *J. Mech. Sci. Technol.*, **30**: 533 (2016);
 - https://doi.org/10.1007/s12206-016-0106-9
- 37. L.Z. Ye, X.J. Zhu, Y. He, T.J. Song, and W. Hu, *Chinese J. Aeronaut*, 34: 508 (2021);
 - https://doi.org/10.1016/j.cja.2020.08.043
- 38. C. Zhu, S. He, M. Shan, and J Chen, *Ultrasonics*, **44**: 349 (2006); https://doi.org/10.1016/j.ultras.2006.07.016
- 39. G.L. Chahine, A. Kapahi, J.K. Choi, and C.T. Hsiao, *Ultrason. Sonochem.*, 29: 528 (2016); https://doi.org/10.1016/j.ultsonch.2015.04.026
- 40. G. Wang, W. Wu, J. J. Zhu, and D. Peng, *Ultrason. Sonochem.*, **79**: 105781 (2021); https://doi.org/10.1016/j.ultsonch.2021.105781
- 41. L. Jing and L. Jian, *J. Eng. Tribology*, **223**: 985 (2009); https://doi.org/10.1243/13506501JET593
- 42. B.N. Mordyuk and G.I. Prokopenko, *Ultrasonics*, **42**: 43 (2004); https://doi.org/10.1016/j.ultras.2004.01.001
- 43. V.M. Nadutov, B.N. Mordyuk, G.I. Prokopenko, and I.S. Gavrilenko, *Ultrasonics*, 42: 47 (2004); https://doi.org/10.1016/j.ultras.2004.01.002
- 44. M. Duraiselva, R. Galun, V. Wesling, B.L. Mordike, R. Reiter, J. Oligmuller, and G. Buvanashekaran, *Mater. Sci. Eng. A*, 454–455: 63 (2007); https://doi.org/10.1016/j.msea.2006.11.002
- 45. H.S. Chen, S.H. Liu, J.D. Wang, and D. Chen, J. Appl. Phys., 101: 103 (2007); https://doi.org/10.1063/1.2734547
- J. Lago, L. Trsko, M. Jambor, F. Novy, O. Bokuvka, M. Mician, and F. Pastorek, *Metals*, 9: 619 (2019), https://doi.org/10.3390/met9060619

- 47. H. Qi, Z. Cheng, D. Cai, L. Yin, Z. Wang, and D. Wen, *J. Mater. Process. Technol.*, **259**: 361 (2018);
 - https://doi.org/10.1016/j.jmatprotec.2018.04.043
- 48. ASTM G32-16; Standard test method for cavitation erosion using vibratory apparatus. ASTM International (West Conshohocken, PA, USA: 2021).
- 49. J.Z. Zhang, W.B. Dai, X.S. Wang, Y.M. Wang, H.T. Yue, Q. L, X.N. Yang, C.G. Guo, and C.Y. Li. J. Mater. Res. Technol., 23: 4307 (2023); https://doi.org/10.1016/j.jmrt.2023.02.028
- Kamal Jayaraj, S. Malarvizhi, and V. Balasubramanian, Defence Technology, 13: 111 (2017); https://doi.org/10.1016/j.dt.2017.03.003
- 51. L. Ropyak, T. Shihab, A. Velychkovych, O. Dubei, T. Tutko, and V. Bilinskyi, Design of a two-layer Al-Al₂O₃ coating with an oxide layer formed by the plasma electrolytic oxidation of Al for the corrosion and wear protections of steel, *Prog. Phys. Met.*, 24, No. 2: 319 (2023); https://doi.org/10.15407/ufm.24.02.319
- 52. M. Szkodo, A. Stanisławska, A. Komarov, and Ł. Bolewski, *Wear*, **474–475**: 203709 (2021); https://doi.org/10.1016/j.wear.2021.203709
- 53. J.B. Cheng, X.B. Liang, B.S. Xu, and Y.X. Wu, J. Mater. Sci., 44: 3356 (2009); https://doi.org/10.1007/s10853-009-3436-5
- 54. Y. Wang, K.Y. Li, F. Scenini, J. Jiao, S.J. Qu, Q. Luo, and J. Shen, Surf. Coat. Technol., 302: 27 (2016); https://doi.org/10.1016/j.surfcoat.2016.05.034
- 55. J.R. Lin, Z. Wang, J.B. Cheng, M. Kang, X.Q. Fu, and S. Hong, *Coatings*, 7: 200 (2017);
- https://doi.org/10.3390/coatings7110200
 56. R.H. Purba, K. Shimizu, K. Kusumoto, T. Todaka, M. Shirai, H. Hara, and J. Ito, Tribol. Int., 159: 106982 (2021);
 - https://doi.org/10.1016/j.triboint.2021.106982
- J.C. Tan, L. Looney, and M.S.J. Hashmi, J. Mater. Process. Tech., 92–93: 203 (1999); https://doi.org/10.1016/s0924-0136(99)00113-2
- 58. K.N. Singh, S.M.A. Ang, K.D. Mahajan, and H. Singh, *Tribol. Int.*, **159**: 106954 (2021); https://doi.org/10.1016/j.triboint.2021.106954
- E. Jonda and L. Łatka, Adv. Sci. Technol. Res. J., 15: 57 (2021); https://doi.org/10.12913/22998624/135979
- E. Jonda, M. Szala, M. Sroka, L. Łatka, and M. Walczak, Appl. Surf. Sci., 608: 155071 (2023); https://doi.org/10.1016/j.apsusc.2022.155071
- X. Ding, X.D. Cheng, X. Yu, C. Li, C.Q. Yuan, and Z.X. Ding, Trans. Nonferrous Met. Soc. China, 28: 487 (2018); https://doi.org/10.1016/S1003-6326(18)64681-3
- 62. J. Cheng, Y.P. Wu, S.S. Zhu, S. Hong, J.B. Cheng, and Y.J. Wang, J. Mater. Res. Technol., 25: 2936 (2023); https://doi.org/10.1016/j.jmrt.2023.06.10936e2947
- 63. C. Suryanarayana and A. Inoue, *Int. Mater. Rev.*, **58**: 131 (2013); https://doi.org/10.1179/1743280412Y.0000000007
- 64. G.Y. Koga, R. Schulz, S. Savoie, A.R.C. Nascimento, Y. Drolet, C. Bolfarini, C.S. Kiminami, and W.J. Botta, *Surf. Coat. Technol.*, **309**: 938 (2016); https://doi.org/10.1016/j.surfcoat.2016.10.057

- 65. L. Qiao, Y. Wu, S. Hong, J. Zhang, W. Shi, and Y. Zheng, Ultrasonics Sonochemistry, 306: 938 (2017);
 - https://doi.org/10.1016/j.ultsonch.2017.04.011
- 66. A. Bandar, Fundamentals of cold spray processing: evolution and future perspectives, *Cold Spray Coatings: Recent Trends Future Perspective* (Ed. P. Cavaliere) (Springer: 2018);
 - https://doi.org/10.1007/978-3-319-67183-3
- 67. M. Kazasidis, S. Yin, J. Cassidy, T. Volkov-Husović, M. Vlahović, S. Martinović, E. Kyriakopoulou, and R. Lupoi, *Surf. Coat. Technol.*, **382**: 125195 (2020); https://doi.org/10.1016/j.surfcoat.2019.125195
- 68. Y. Shuo, E.J. Ekoi, T.L. Lupton, D.P. Dowling, and R. Lupoi, *Mater. Des.*, **126**: 305 (2017);
 - https://doi.org/10.1016/j.matdes.2017.04.040
- Krebs, F. Gärtner, and T. Klassen, J. Therm. Spray Technol., 24: 126 (2015); https://doi.org/10.1007/s11666-014-0161-7
- F. Lomello, F. Sanchette, F. Schuster, M. Tabarant, and A. Billard, Surf. Coat. Technol., 224: 77 (2013); https://doi.org/10.1016/j.surfcoat.2013.02.051
- B. Navinsek, P. Panjan, and I. Milosev, Surf. Coat. Technol., 97: 182 (1997); https://doi.org/10.1016/S0257-8972(97)00393-9
- 72. S. Han, J.H. Lin, J.J. Kuo, J.L. He, and H.C. Shih, Surf. Coat. Technol., 161: 20 (2002); https://doi.org/10.1016/S0257-8972(02)00392-4
- 73. F. da S. Severo, C.J. Scheuer, R.P. Cardoso, and S.F. Brunatto, *Wear*, **428–429**: 162 (2019);
 - https://doi.org/10.1016/j.wear.2019.03.009
- 74. C.L. Wu, S. Zhang, C.H. Zhang, H. Zhang, and S.Y. Dong, J. Alloys Compounds, 698: 761 (2017);
 - http://dx.doi.org/10.1016/j.jallcom.2016.12.196
- 75. K.H. Lo, F.T. Cheng, C.T. Kwok, and H.C. Man, Surf. Coat. Technol., 165: 258–267 (2003);
 - https://doi.org/10.1016/S0257-8972(02)00739-9
- 76. S. Zhang, C.L.Wu, C.H. Zhang, M. Guan, and J.Z. Tan, Optics Laser Technol., 84: 2331 (2016);
 - https://doi.org/10.1016/j.optlastec.2016.04.011
- 77. C.T. Kwok, F.T. Cheng, and H.C. Man, Surf. Coat. Technol., 145: 194 (2001); https://doi.org/10.1016/S0257-8972(01)01293-2
- 78. S.P. Gadag, M.N. S.P. Gadag, and M.N. Srinivasan, *Mater. Process. Technol.*, 51: 150 (1995);
 - https://doi.org/10.1016/0924-0136(94)01601-V
- 79. E. Wolowiec-Korecka, Carburising and Nitriding of Iron Alloys (Springer: 2024).
- 80. D. Liedtke, U. Baudis, J. Boßlet, U. Huchel, H.K. Westkamp, W. Lerche, and H.J. Spies, *Nitriding and Nitrocarburizing on Iron Materials* (Tokyo: AGNE Gijutsu Center: 2013).
- M. Drouet and E. Le Bourhis, Materials, 16: 4704 (2023); https://doi.org/10.3390/ma16134704
- 82. A.N. Allenstein, C.M. Lepienski, A.J.A. Buschinelli, and S.F. Brunatto, Wear, 309: 159 (2014);
 - https://doi.org/10.1016/j.wear.2013.11.002
- 83. I. Mitelea, E. Dimian, I. Bordeaşu, and C. Crăciunescu, *Ultrasonics Sonochem.*, 21: 1544 (2014);
 - https://doi.org/10.1016/j.ultsonch.2014.01.005

- 84. H.C. Man, Z.D. Cui, T.M. Yue, and F.T. Cheng, *Mater. Sci. Eng. A*, 355: 167 (2003); https://doi.org/10.1016/S0921-5093(03)00062-5
- 85. S.P. Gadag and M.N. Srinivasan, J. Mater. Process. Technol., **51**: 150 (1995); https://doi.org/10.1016/0924-0136(94)01601-V
- 86. B.G. Giren, Surf. Eng., 14: 325 (1998); https://doi.org/10.1179/sur.1998.14.4.325
- 87. C.T. Kwok, H.C. Man, and F.T. Cheng, Surf. Coat. Technol., 126: 238 (2000); https://doi.org/10.1016/S0257-8972(00)00533-8
- 88. C.H. Tang, F.T. Cheng, and H.C. Man, Surf. Coat. Technol., 182: 300 (2004); https://doi.org/10.1016/j.surfcoat.2003.08.048
- 89. R.S. Mishra and Z.Y. Ma, *Mater. Sci. Eng. R*, **50**: 1 (2005); https://doi.org/10.1016/j.mser.2005.07.001
- 90. S. Park, C.G. Lee, H.N. Han, S.J. Kim, and K. Chung, Met. Mater. Int., 14: 47 (2008); https://doi.org/10.3365/met.mat.2008.02.047
- A.K. Lakshminarayanan and V. Balasubramanian, *Mater. Sci. Eng. A*, **539**: 143 (2012); https://doi.org/10.1016/j.msea.2012.01.071
- 92. H.A. Abdollah-Zadeh, S.S. Rezaei-Nejad, H. Assadi, S.M.M. Hadavi, K. Chung, and M. Shokouhimehr, *Appl. Surf. Sci.*, 308: 184 (2014); https://doi.org/10.1016/j.apsusc.2014.04.132
- 93. X. Zhang and L. Fang, Wear, 253: 1105 (2002); https://doi.org/10.1016/S0043-1648(02)00168-0
- 94. G.W. Lorimer, F. Hasan, J. Iqbal, and N. Ridley, *Br. Corros. J.*, **21**: 244 (1986); http://dx.doi.org/10.1179/000705986798272046
- 95. A. Al-Hashem and W. Riad, *Mater. Characterization*, **48**: 37 (2002); https://doi.org/10.1016/S1044-5803(02)00196-1
- 96. A. Al-Hashem and J. Carew, *Desalination*, **150**: 255 (2002); https://doi.org/10.1016/S0011-9164(02)00981-5
- 97. S. Thapliyal and D.K. Dwivedi, *Wear*, 376–377: (2017); https://doi.org/10.1016/j.wear.2017.01.030
- 98. J.H. Chen, P.H. Hua, P.N. Chen, C.M. Chang, M.C. Chen, and W. Wu, *Mater. Lett.*, **62**: 2490 (2008); https://doi.org/10.1016/j.matlet.2007.12.038
- 99. Z.D. Wan, Z.L. Yi, Y. Zhao, S.C. Zhang, Q. Li, J. Lin, and A.P. Wu, Mater. Design, 245: 113274 (2024); https://doi.org/10.1016/j.matdes.2024.113274
- 100. P. Binande, H.R. Shahverdi, and A. Farnia, J. Mater. Res. Technol., 33: 9092 (2024);
 - https://doi.org/10.1016/j.jmrt.2024.11.231
- 101. M. Ardeshir, M. Yousefpour, S.M.S. Nourbabksh, and M. Bozorg, *Heliyon*, 10: 41062 (2024);
 - https://doi.org/10.1016/j.heliyon.2024.e41062
- 102. I. Mitelea, T. Bena, I. Bordeașu, I.D. Uțu, and C.M. Crăciunescu, $Metall\ Mater.\ Trans.\ A,\ 50:\ 3767\ (2019);$
 - https://doi.org/10.1007/s11661-019-05287-w
- 103. I. Adhiwiguna, N. Nobakht, and R. Deike, Metals, 14: 915 (2024); https://doi.org/10.3390/met14080915
- 104. K. Salonitis, M. Jolly, E. Pagone, and M. Papanikolaou, *Energies*, 12: 2557 (2019);
 - https://doi.org/10.3390/en12132557

- 105. K. Jhaveri, G.M. Lewis, J.L. Sullivan, and G.A. Keoleian, Sustainable Mater. Technol., 15: 1 (2018);
 - https://doi.org/10.1016/j.susmat.2018.01.002
- 106. E. Riemschneider, I. Bordeaşu, I. Mitelea, I.D. Uţu, and C.M. Crăciunescu, *Mater. Today: Proc.*, 45: 4157 (2021);

https://doi.org/10.1016/j.matpr.2020.11.929

Received 07.02.2025 Final version 19.08.2025

Б.М. Мордюк¹, М.О. Васильєв¹, С.М. Волошко², О.А. Вислий²

- ¹ Інститут металофізики ім. Г.В. Курдюмова НАН України, бульв. Академіка Вернадського, 36, 03142 Київ, Україна
- ² Національний технічний університет України
- «Київський політехнічний інститут імені Ігоря Сікорського, просп. Берестейський, 37, 03056 Київ, Україна

ПІДВИЩЕННЯ СТІЙКОСТИ ДО УЛЬТРАЗВУКОВОЇ КАВІТАЦІЙНОЇ ЕРОЗІЇ МЕТАЛЕВИХ ДЕТАЛЕЙ ШЛЯХОМ МОДИФІКУВАННЯ ПОВЕРХНІ

Розглянуто поточний розвиток оброблень поверхні, спрямованих на підвищення стійкості до кавітаційної ерозії (КЕ) металевих виробів, які працюють в умовах вібрації в рідких середовищах. Також розглянуто ультразвукове кавітаційне тестування, яке є зручним й експресним методом оцінювання кавітаційної стійкості матеріалів. Стійкість до КЕ зразків металу переважно перевіряється за допомогою типового ультразвукового вібраційного приладу відповідно до стандарту випробувань ASTM G32-10. Описано та проаналізовано фізичний механізм кавітаційної деструкції поверхні на основі утворення пароподібних порожнин. Цей аналіз дає змогу ліпше зрозуміти вплив методів оброблення поверхні та їхніх параметрів на структуру і механічні властивості приповерхневої області для підвищення захисту від руйнівних ефектів кавітації. Наведено приклади ефективних методів поліпшення властивостей поверхні різних металевих матеріалів, а саме: методи нанесення покриттів, у тому числі мікродугове оксидування, дугове напорошення, високошвидкісне кисневе осадження, холодне напорошення, катодно-дугове плазмове осадження, лазерне легування поверхні й азотування. Крім того, зроблено висновок, що такі методи модифікування поверхні, як лазерне оброблення поверхні, оброблення фрикційним перемішуванням і зварювання/плавлення вольфрамовим електродом в інертному газі також є ефективними інгібіторами КЕ.

Ключові слова: кавітація, поверхневе оброблення, покриття, ерозійна стійкість, ультразвукова вібрація, кавітаційні випробування.